https://doi.org/10.5194/egusphere-2026-6871
Preprint. Discussion started: 13 November 2026
© Author(s) 2026. CC BY 4.0 License.

# Reanalysis evaluation of the Atlantic meridional overturning circulation variations

Sukun Cheng[1,2], Susanna Winkelbauer[3], Julia Araujo[4], Magdalena Balmaseda[5], Romain Bourdallé-Badie[6], Yumeng Chen[1,2], Gaël Forget[7], Doroteaciro Iovino[8], Chunxue Yang[4], Keith Haines[1,2]

1. Department of Meteorology, University of Reading, Reading, UK
2. National Centre for Earth Observation, Reading, UK
3. Department of Meteorology and Geophysics, University of Vienna, Vienna, Austria
4. Institute of Marine Sciences, National Research Council of Italy (CNR-ISMAR), Rome, Italy
5. European Centre for Medium-Range Weather Forecasts, Reading, UK
6. Mercator Ocean International, Toulouse, France
7. Department of Earth, Atmospheric and Planetary Sciences, Massachusetts Institute of Technology, Cambridge, MA, USA
8. CMCC Foundation – Euro-Mediterranean Centre on Climate Change, Bologna, Italy

Correspondence: Sukun Cheng (s.cheng@reading.ac.uk) and Keith Haines (k.haines@reading.ac.uk)

**Abstract**

We evaluate the Atlantic Meridional Overturning Circulation (AMOC) in five global ocean reanalyses (C-GLORSv8, GLORYS4v2, GLOSIA9v1, SODA3 and ECCOv4r4), comparing estimated overturning transports against the RAPID, OSNAP and SAMBA observing arrays at 26.5°N, ~53–60°N and 34.5°S over the altimeter era. AMOC transports are computed directly from each reanalysis's meridional velocity field, in both depth and density coordinates, in a consistent evaluation framework. Time-mean AMOC strengths in the three NEMO-based reanalyses are within 2 Sv of the observed values at RAPID and OSNAP, while SODA3 and ECCOv4r4 have weaker mean AMOC strengths at OSNAP; discrepancies are larger at SAMBA, both between products and against the observations. Seasonal cycles are well reproduced in the North Atlantic (RAPID and OSNAP) and less so at SAMBA. Reanalyses agree well with observed deseasonalised AMOC variability at RAPID and more moderately at OSNAP, with monthly anomaly correlations of 0.63–0.85 and 0.26–0.58, respectively. All reanalysis products show a weak long-term decline of AMOC strength at RAPID, primarily due to the well reproduced decline 2003–2012. No consistent trends are found between products at OSNAP or SAMBA. Overall, the comparison supports the use of reanalyses for monitoring upper-cell AMOC variability, particularly at RAPID, while showing larger uncertainties in the deep overturning structure and in the South Atlantic. The RAPID agreement also motivates their consideration as candidate ocean initial states for coupled decadal predictions.

## 1. Introduction

The Atlantic Meridional Overturning Circulation (AMOC) plays a critical role in Earth's climate system. It transports substantial heat northwards in the Atlantic Ocean, and helps to maintain the deep cold sub-thermocline water masses that fill

https://doi.org/10.5194/egusphere-2026-6871
Preprint. Discussion started: 13 November 2026
© Author(s) 2026. CC BY 4.0 License.

most of the deep oceans throughout the globe (e.g. Pérez et al., 2013; Frajka-Williams et al., 2019; Bryden et al., 2020; Rousselet et al., 2020, 2021; Williams et al., 2021). Theoretical modelling studies (Stommel, 1961; Weijer et al., 2019, 2020) as well as paleo evidence (Lynch-Stieglitz et al., 2007; Böhm et al., 2015) suggest that the AMOC could substantially decline from its current state, leading to major consequences for the climate of much of the Northern Hemisphere (Vellinga and Wood, 2002; Jackson et al., 2015; Bellomo et al., 2021). This sensitivity has motivated AMOC monitoring arrays across the Atlantic. The first complete array, the RAPID-MOCHA-WBTS observing system (hereafter RAPID) at approximately 26.5°N (Cunningham et al., 2007; Johns et al., 2011; Smeed et al., 2018), has been in place since 2004. This revealed strong AMOC variability on both short and long timescales and challenged the ocean and climate modelling community to understand and reproduce that variability (Jackson et al., 2019; Buckley and Marshall, 2016).

Improved estimates of AMOC strength and variability are also important for better climate monitoring and prediction. The AMOC integrates the atmospheric forcing and oceanic processes over large spatial scales and therefore provides a physically meaningful indicator of changes occurring within the coupled climate system. Meanwhile, the ocean's long-term memory means that its state contains information relevant to predictions on interannual-to-decadal timescales. Of great practical importance is the potential to reproduce AMOC variability on longer timescales, and modelling studies suggest that AMOC transport may be predictable, offering some predictability of North Atlantic regional climate. Smith et al. (2007) pioneered a decadal forecasting system based on initialising the ocean component of a coupled model. Many subsequent studies have suggested that initialising the ocean state associated with the AMOC transports may be critical to gaining predictability on these longer timescales (Msadek et al., 2010; Zhang et al., 2019).

Atmospheric reanalysis products, such as those from ECMWF (Hersbach et al., 2020), have become established tools for understanding atmospheric circulation and processes and testing forecasting capabilities through hindcasts (Hamill et al., 2006). Ocean reanalyses similarly offer spatially and temporally complete estimates of the ocean state, which should allow AMOC variability and transports to be examined on short and long timescales, including where direct observations are unavailable. While a few studies have tried to assess individual reanalysis circulations and transports (Forget, 2010; Haines et al., 2012; Valdivieso et al., 2014; Evans et al., 2017; Kostov et al., 2021), most multi-product ocean reanalysis comparisons have focused on more directly observable metrics such as water mass properties, ocean heat content or sea level (Balmaseda et al., 2015; Jackson et al., 2019; Storto et al., 2019). Previous AMOC comparisons of one-degree-resolution, long-period reanalyses used in decadal forecasting, mostly poorly constrained by ocean observations, found large discrepancies among products (Karspeck et al., 2017). More recently, a comparison of European reanalyses in the 7th Copernicus Ocean State Report found a mean South Atlantic overturning similar to observation-based estimates (Baker et al., 2023). Raganato et al. (2026) compared four ocean reanalyses with forced ocean–sea ice simulations near 26°N, 58°N and 34°S in the Atlantic Ocean, focusing on the consistency of AMOC strength, freshwater transport and gyre circulation; their gyre diagnostics show a robust positive relationship between the means of gyre strength and AMOC strength near 26°N across datasets. However, an evaluation of the latest reanalyses against the Atlantic monitoring arrays, using diagnostics consistent with each array, is still lacking.

https://doi.org/10.5194/egusphere-2026-6871
Preprint. Discussion started: 13 November 2026
© Author(s) 2026. CC BY 4.0 License.

This study is carried out within the framework of the Ocean Decade Marine Environment Reanalyses Evaluation Project (MER-EP; Yang et al., 2026), which aims to systematically evaluate and intercompare global ocean and marine reanalyses across a broad range of variables, processes and user-oriented applications. MER-EP builds upon earlier coordinated ocean reanalysis intercomparison efforts, most notably the Ocean Reanalyses Intercomparison Project (ORA-IP; Balmaseda et al., 2015). Within MER-EP's user-oriented, fitness-for-purpose framework, this study assesses the representation of AMOC strength and variability by comparing transport estimates from observations and the most recent global ocean reanalyses covering the altimeter era (1993–present). We compare the AMOC in reanalyses with observations at the RAPID array at 26.5°N, the OSNAP array near 57°N and the SAMBA array at 34.5°S, and examine the overturning in depth and density coordinates following the observations and extending over longer time periods. By evaluating reanalysed transports against the increasingly long observational record, we aim to determine the extent to which reanalyses agree with each other and with observed AMOC variability, identify where the main transport and structural differences occur, and assess the implications for the use of reanalyses in climate monitoring and decadal prediction. This provides a basis for evaluating whether current reanalysis products adequately capture the meridional overturning circulation changes that are relevant both to detecting climate change and to constructing physically consistent initial states for decadal forecasting.

Section 2 describes the product datasets, focusing on the post-altimeter period from 1993 onwards, and the AMOC observational arrays used for comparison. Section 3 discusses different AMOC calculation methodologies within the reanalyses, and how they compare with the observational data treatment. Section 4 focuses on the time-mean AMOC and its vertical structure throughout the Atlantic basin and at the monitored sections. Section 5 focuses on the time variability of the AMOC: first the seasonal cycle, then the deseasonalised monthly variability at each section, and finally the longer-term tendencies across the three sections. Section 6 provides discussion and conclusions.

## 2. Data

### 2.1 Ocean reanalyses

We analyse monthly fields from five global ocean reanalysis products: three reanalyses are from the latest generation of Copernicus Marine Service (formerly Copernicus Marine Environment Monitoring Service, CMEMS) Global Ocean Reanalysis Ensemble Product (GREP): C-GLORSv8, GLORYS4v2 (Bourdallé-Badie et al., 2026) and GLOSIA9v1, and two US-based reanalyses, SODA3 and ECCOv4r4. The GREP products share the Nucleus for European Modelling of the Ocean (NEMO) ORCA025 grid (quarter-degree resolution) but use different data assimilation systems, allowing comparison among similar reanalysis configurations. Earlier versions of these GREP products are discussed in Jackson et al. (2019) and von Schuckmann and Le Traon (2022). SODA3 (v3.15.2; Carton et al., 2018) and ECCOv4r4 (Forget et al., 2015; ECCO Consortium, 2021a, b) are included as complementary products with different ocean models, grids and assimilation frameworks. ECCOv4r4 particularly provides a dynamically consistent ocean state estimate over the full historical trajectory of observations (4DVar), rather than a sequential assimilation reanalysis (Forget et al., 2015), although at one-degree

https://doi.org/10.5194/egusphere-2026-6871
Preprint. Discussion started: 13 November 2026
© Author(s) 2026. CC BY 4.0 License.

resolution. Table 1 summarises the products. Monthly mean velocity, temperature and salinity fields are used to compute the AMOC in depth and density space (Sect. 3).

**Table 1: Summary of ocean reanalysis products.**

| Dataset | C-GLORSv8 | GLORYS4v2 | GLOSIA9v1 | SODA3.15.2 | ECCOv4r4 |
|---|---|---|---|---|---|
| Producer | CMCC | Mercator Ocean International | UK Met Office | University of Maryland | ECCO Consortium / MIT–JPL |
| Time period | 1987–2023 | 1993–2023 | 1994–2023 | 1993–2023 | 1992–2017 |
| Ocean model | NEMO v3.6 with LIM2 | NEMO v3.6 | NEMO v4.04 | GFDL MOM5 with SIS1 | MITgcm |
| Native grid | ORCA025 tripolar | ORCA025 tripolar | ORCA025 tripolar | Arakawa B-grid tripolar | LLC90 |
| Equation of state | EOS-80 | EOS-80 | TEOS-10 | EOS-80 | EOS-80 |
| Resolution | ¼°, 75 levels | ¼°, 75 levels | ¼°, 75 levels | ¼°, 50 levels | ≈1°, 50 levels |
| Atmospheric forcing | ERA5 | ERA5 | ERA5 | ERA5 | ERA-Interim, with optimised adjustments to atmospheric forcing (excluding wind speed and surface pressure) |
| Data assimilation | Multivariate 3D-Var (OceanVar) | SEEK / reduced-order Kalman filter | 3D-Var FGAT (NEMOVAR) | Optimal Interpolation | Long-window adjoint least-squares state estimation |
| Assimilated observations | In-situ T/S, SLA, SST, SIC and SIT | In-situ T/S, SLA, SST and SIC | In-situ T/S, SLA, SST and SIC | In-situ T/S, in-situ and satellite SST | In-situ T/S, SST, SSS, SLA/SSH, SIC, global mean sea level, ocean bottom pressure, T/S climatology, mean dynamic topography |

### 2.2 Observational estimates of the AMOC

We evaluate the reanalyses against three trans-basin arrays, RAPID, OSNAP and SAMBA (Table 2). RAPID provides normal overturning velocity fields in both depth and density coordinates, OSNAP in density space only. SAMBA provides the evaluated peak overturning transports rather than full velocity fields. The three cross-sections are shown in Fig. 1a.

https://doi.org/10.5194/egusphere-2026-6871
Preprint. Discussion started: 13 November 2026
© Author(s) 2026. CC BY 4.0 License.

#### 2.2.1 RAPID (26.5°N)

The AMOC at 26.5°N has been monitored continuously since 2004 by the RAPID array, producing a full-depth estimate of the meridional overturning (Cunningham et al., 2007; Kanzow et al., 2007; McCarthy et al., 2015). The array reports the overturning as the sum of three measured contributions: the Florida Straits (Gulf Stream) transport from the submarine cable, the ERA5 wind-driven Ekman transport, and the geostrophic upper mid-ocean transport between the western and eastern boundaries. The depth–longitude velocity section is a gridded reconstruction built from these boundary measurements, not a directly measured trans-basin field. McCarthy et al. (2015) estimate RMS errors of 1.5 Sv (10-day) and 0.9 Sv (annual) from April 2004 to October 2012 (Table 2; Appendix A.1).

#### 2.2.2 OSNAP array (~53–60°N)

The overturning in the subpolar North Atlantic is monitored by the OSNAP (Overturning in the Subpolar North Atlantic Program) array, a trans-basin line of moorings and gliders spanning from the Labrador shelf to the Scottish shelf and split into a western section across the Labrador Sea (OSNAP West) and an eastern section from Greenland to Scotland (OSNAP East; Li et al., 2017; Lozier et al., 2019). Because isopycnals slope strongly across the section, the overturning is provided in density coordinates. No error budget of the real array is available, so we use the observing system simulation experiment (OSSE) of Li et al. (2017) instead (Appendix A.1), which gives 30-day RMS differences of 1.38 Sv (East) and 0.72 Sv (West). As with the RAPID depth–longitude section (Sect. 2.2.1), the gridded OSNAP velocity field is a mapped reconstruction from the sparse mooring array rather than a directly measured, spatially continuous field (Li et al., 2021, Fig. 1b).

#### 2.2.3 SAMBA array (34.5°S)

The AMOC at 34.5°S is monitored by the SAMBA (South Atlantic MOC Basin-wide array), a trans-basin line of pressure-equipped inverted echo sounders (PIES), current- and pressure-recording inverted echo sounders (CPIES), and moorings maintained under the SAM and SAMOC-Fr programmes (Meinen et al., 2018; Kersalé et al., 2020). There are two NOAA/AOML distributions, both delivered as AMOC anomalies rather than absolute transports. Meinen et al. (2018) provide the total upper-cell MOC anomaly and its density, bottom-pressure and Ekman constituents as daily values relative to a reference mean of 14.7 Sv; a ~2.8-year gap (Table 2) splits the record into two segments (2009–2010 and 2013–2017). The upper-cell MOC strength is identified as the maximum of the pressure-space streamfunction between the surface (0 dbar) and 2000 dbar. The second distribution, Kersalé et al. (2020), uses fixed pressure interfaces and is described in Appendix A.1.

For the reanalysis comparison, we use the Meinen et al. (2018) product because its upper-cell MOC definition is more directly comparable with our reanalysis diagnostics, in which AMOC strength is defined as the maximum of the overturning streamfunction. This is also consistent with the diagnostic used at the other observational sections. Meinen et al. (2013)

https://doi.org/10.5194/egusphere-2026-6871
Preprint. Discussion started: 13 November 2026
© Author(s) 2026. CC BY 4.0 License.

estimate, from an error budget for the 2009–2010 pilot array, a random error of 5.9 Sv for unfiltered daily values and a time-mean bias of up to 4.4 Sv; Meinen et al. (2018) followed the random error estimate of 5.9 Sv (Table 2; Appendix A.1).

**Table 2: Summary of sectional observations at RAPID, OSNAP and SAMBA.**

| **Monitoring section** | **RAPID-MOCHA-WBTS** | **OSNAP** | **SAMBA** |
|---|---|---|---|
| **Nominal position** | 26.5°N | subpolar North Atlantic, ≈57°N | 34.5°S |
| **Data release** | v2024.1a (Moat et al., 2026) | May 2025 (Fu et al., 2025a, b) | Meinen et al. (2018) |
| **Period** | 2 April 2004 – 27 March 2024 | 1 August 2014 – 31 July 2022 | 18 March 2009 – 29 April 2017 (gap 3 December 2010 – 4 September 2013) |
| **Temporal resolution** | Twice-daily (10-day low-pass filtered), averaged to monthly | Monthly (native) | Daily, averaged to monthly |
| **Published error estimates** | RMS error 1.5 Sv (10-day), 0.9 Sv (annual), no bias estimate (McCarthy et al., 2015) | No error budget of the real array; model-based OSSE: RMS difference 1.38 / 0.72 Sv, mean difference −1.92 / +0.13 Sv, East / West (Li et al., 2017) | Random error 5.9 Sv (daily), bias up to 4.4 Sv (Meinen et al., 2013) |

## 3. Methodology

We diagnose AMOC directly from the meridional velocity of each reanalysis and compare the section-integrated transports with the observations described in Sect. 2. A common transport framework is used wherever possible (Appendix A.2) so that differences among products primarily reflect differences in the reanalysed circulation rather than diagnostic methods.

### 3.1 Overturning streamfunction and AMOC strength

The overturning streamfunction, Ψ, is diagnosed from cross-section normal velocity in depth and density coordinates. Depth space separates the vertically stacked northward upper limb, southward North Atlantic Deep Water (NADW) return flow and northward Antarctic Bottom Water (AABW) bottom cell, and follows the depth (pressure) convention of the RAPID and SAMBA estimates. Where isopycnals are flat across a section, density levels coincide with depth levels and the two streamfunctions are equivalent. Where isopycnals slope, as in the subpolar North Atlantic, density space also captures horizontal circulations at different densities, whose northward and southward branches partly cancel along depth levels; across OSNAP East this contribution is about 40 % of the maximum density-space overturning (Zhang and Thomas, 2021). The OSNAP comparison is therefore made in $\sigma_0$ space, following the observational convention of Lozier et al. (2019); at

https://doi.org/10.5194/egusphere-2026-6871
Preprint. Discussion started: 13 November 2026
© Author(s) 2026. CC BY 4.0 License.

RAPID and SAMBA, AMOC time series use depth space, and time-mean profiles are shown in both depth and $\sigma_0$ space. In depth space,

$$\Psi(z,t) = \int_{z_{\mathrm{bot}}}^{z} \int_{x_w}^{x_e} v\,(x,z',t)\,dx\,dz'\,, \tag{1}$$

where $t$ is time, $x$ is the eastward coordinate, $z$ is depth (positive downward), and $v$ is cross-section normal velocity, positive northwards. In density space, transport in depth is first gathered into density classes and then accumulated,

$$\Psi(\sigma,t) = \int_{\sigma_{\min}}^{\sigma} \int_{x_w}^{x_e} v\,(x,\sigma',t)\,\frac{\partial z}{\partial \sigma'}\,dx\,d\sigma'\,, \tag{2}$$

where $\sigma$ denotes the density coordinate (in this study $\sigma_0$, the potential density anomaly referenced to the surface), and the inner integral is the section volume transport per unit density (Appendix A.3). AMOC strength is defined as the maximum of the upper-cell overturning streamfunction (Appendix A.3):

$$\mathrm{AMOC}(t) = \max[\Psi(\bullet,t)]\,, \tag{3}$$

An observation-style RAPID reconstruction using METRIC (Castruccio, 2021; Danabasoglu et al., 2021) was also tested (not shown). However, at the resolution of the reanalysis products considered here, the METRIC reconstructed transports differed significantly from those obtained by direct velocity integration in the mean, seasonal cycle and temporal variability. The principal analysis therefore uses the directly integrated model velocity fields.

### 3.2 Mean seasonal cycle, anomalies and comparison periods

We assess the mean seasonal cycle (MSC) of each product separately. Removing this MSC to define monthly anomalies then provides a more specific comparison for the reanalysis products, as seasonal variability is expected to be strongly correlated among products, largely through common atmospheric forcing. The MSC of the AMOC is calculated as the mean for the corresponding calendar month using complete annual cycles, so that each calendar month receives the same number of contributing years. The deseasonalised monthly anomalies are then obtained over the full product time series by removing the MSC.

The model–observation comparison periods are 04/2004–03/2023 at RAPID (ending with the last complete April–March cycle of the reanalyses available here) and 08/2014–07/2022 at OSNAP; these are also complete annual-cycle MSC periods. Products whose records do not span a full comparison period are retained using their available overlapping period. At SAMBA, the comparison uses the two observed segments, 03/2009–12/2010 and 09/2013–04/2017 (Appendix A.3).

### 3.3 Statistical comparison, trends and inter-product spread

Mean-state comparisons consider the time-mean streamfunction, AMOC strength, the depth or density of the overturning maximum, and the mean difference between each reanalysis and the corresponding observational estimate.

https://doi.org/10.5194/egusphere-2026-6871
Preprint. Discussion started: 13 November 2026
© Author(s) 2026. CC BY 4.0 License.

Temporal agreement is assessed from matched monthly values using the Pearson correlation (r) of deseasonalised anomalies, the root-mean-square difference (RMSD) between each reanalysis and the reference series, its centred form (CRMSD), and the standard deviation (std) of the anomaly series. We use difference rather than error throughout, because neither the reanalyses nor the observational estimates provide a reference truth (Appendix A.1), and the same statistic is also applied between pairs of reanalysis products. Statistics use matched valid months within the comparison periods, excluding observation gaps. For the short, discontinuous SAMBA record, r, RMSD and std are computed over the matched valid months in both observed segments, using the observational harmonic seasonal fit and the reanalysis 2004–2017 MSCs defined in Appendix A.3. These comparisons are interpreted descriptively and are not used to rank the products.

Inter-product spread is calculated as the std across the reanalysis ensemble. We examine both the spread in AMOC strength and, where useful, the spread after each product's own seasonal cycle has been removed. The latter reduces the influence of persistent differences in mean AMOC strength and highlights agreement in temporal variability. Finally, linear trends are fitted to the monthly anomalies by ordinary least squares (OLS) and interpreted descriptively (Appendix A.3).

## 4. Time-mean AMOC transports

This section evaluates time-mean AMOC metrics in these reanalyses across the Atlantic basin and then at the three monitored sections, in depth and $\sigma_0$ coordinates.

### 4.1 Atlantic basin overturning

Figure 1a shows the locations of the RAPID, OSNAP and SAMBA monitoring arrays. Figure 1b shows the time-mean Atlantic overturning streamfunctions for each reanalysis from 66°N to 35°S in depth space, averaged over a common period, 1994–2017. Depth-level results are similar north of 20°N. ECCOv4r4, which is dynamically consistent but of lower resolution, tends to show slightly weaker peak values. All products have significant reversed bottom cells of AABW, and some coherence of overturning cells across latitudes, although with significant weakening from 35°N into the subpolar gyre, except for ECCOv4r4. All products except ECCOv4r4 show some local strengthening of the overturning cell near the Equator at ~1000 m depth, likely due to the greater sensitivity of the equatorial thermocline to assimilation-induced adjustments. Most cells weaken in the South Atlantic, although GLORYS4v2 maintains a more coherent and significantly stronger overturning cell down to 35°S.

Figure 1c shows the corresponding overturning in $\sigma_0$ space. The northern and southern subtropical gyre circulations at lower densities both become clearly separate and coherent in all products. The denser overturning cells are more coherent across latitudes than they are in depth space, especially remaining strong between the subtropical and subpolar gyres. Several products still show local disturbances near the Equator, and most show continuous overturning cells throughout the South Atlantic, again with GLORYS4v2 showing the strongest overturning in southern latitudes.

https://doi.org/10.5194/egusphere-2026-6871
Preprint. Discussion started: 13 November 2026
© Author(s) 2026. CC BY 4.0 License.

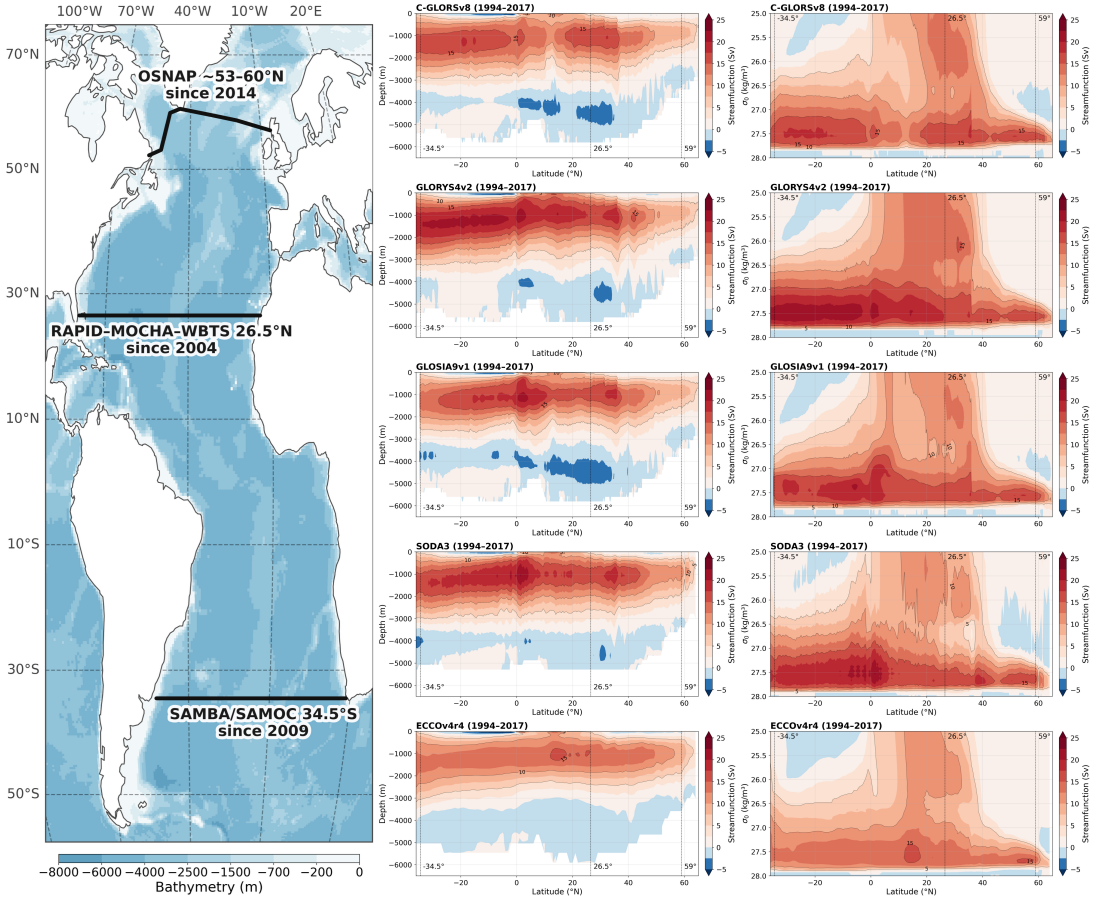



**Figure 1: Locations of the AMOC monitoring arrays and time-mean Atlantic overturning structure. (a) RAPID, OSNAP and SAMBA monitoring sections shown over Atlantic bathymetry. (b) Time-mean Atlantic meridional overturning streamfunction in depth coordinates for five reanalysis products, calculated by integrating section meridional velocity from bottom upwards. (c) Corresponding overturning streamfunction in $\sigma_0$ coordinates. All products are averaged over the common period 1994–2017.**

## 4.2 RAPID AMOC comparisons

Figure 2 shows the time-mean vertical overturning streamfunctions at the 26.5°N RAPID section in depth space (Fig. 2a) and $\sigma_0$ space (Fig. 2b), overlaying all reanalysis products, along with observational profiles from the RAPID array 04/2004–03/2023 (Moat et al., 2026). Some reanalysis averaging periods are slightly reduced where they end before this time, as indicated in Table 1. The most obvious discrepancies in depth space are the significant bottom cells in most products, absent in the RAPID analysis, and shallower southward return flows. Two measures of the AMOC mean strength are given in the legend: one is the mean peak-AMOC, the time mean of the monthly AMOC strengths; the other is the peak mean-AMOC, the maximum of the time-mean vertical overturning streamfunction profile. The former is larger than or equal to the latter, and the two can differ if the depth or density of the monthly maximum varies over time. In depth space, the mean peak-AMOC is only very slightly higher than the peak mean-AMOC. In most reanalysis products, except GLORYS4v2, these

https://doi.org/10.5194/egusphere-2026-6871
Preprint. Discussion started: 13 November 2026
© Author(s) 2026. CC BY 4.0 License.

peaks are 1–2 Sv lower than RAPID array values; however, the total mean southward flow of NADW, integrated upward from the deep cell minima (~4300–4500 m) to the AMOC peak, is stronger: 18.3–19.4 Sv in C-GLORSv8, GLOSIA9v1, GLORYS4v2 and SODA3, compared with 17.9 Sv for RAPID, and 15.7 Sv in ECCOv4r4. The RAPID-style AMOC calculation itself has uncertainties and is particularly sensitive to the choice of deep reference level (e.g., Sinha et al., 2018). The large deviation of the overturning profile in ECCOv4r4 below 3000 m could be due to its relatively coarser vertical resolution or the use of a different ocean model. The bottom flows are still largely unconstrained by observations in all these products.

In $\sigma_0$ space, both the gyre and overturning cells are now distinguished. The AMOC strengths are mostly higher than in depth space and are generally closer to the RAPID array estimates. Differences in peak values compared with RAPID reach 2 Sv in GLOSIA9v1 and ECCOv4r4. In the reanalyses, the mean peak-AMOC is now up to 0.6 Sv higher than the peak mean-AMOC, suggesting some variability in the peak AMOC density, although the two are almost equal in the RAPID array estimate. All products slightly underestimate the highest density of the NADW return flow compared with RAPID, again because these deep flows are poorly constrained even with the Argo data.

Figure 3 shows the time-mean velocity and density cross sections for all products over the RAPID reference period (04/2004 to 03/2023), with ECCOv4r4 shown over a shorter period (04/2004 to 03/2017). The southward geostrophic flow right across the section in the upper thermocline, the northward Gulf Stream on the upper western boundary, and the deeper southward western boundary currents are clear in all products, although spatial scales differ greatly. Most products have some deep and broad boundary currents on the eastern boundary which are not seen in the RAPID array. The ¼° reanalyses also show a northward flow below 1000 m adjacent to the southward deep western boundary current, and a banded velocity structure reaching into the basin, often aligned with topography, which would not be resolved by the RAPID array. Some density reversals in the deep ocean can be seen in SODA3 in $\sigma_0$ space, associated with salinity anomalies at 3000–4000 m in the eastern basin (not shown).

https://doi.org/10.5194/egusphere-2026-6871
Preprint. Discussion started: 13 November 2026
© Author(s) 2026. CC BY 4.0 License.

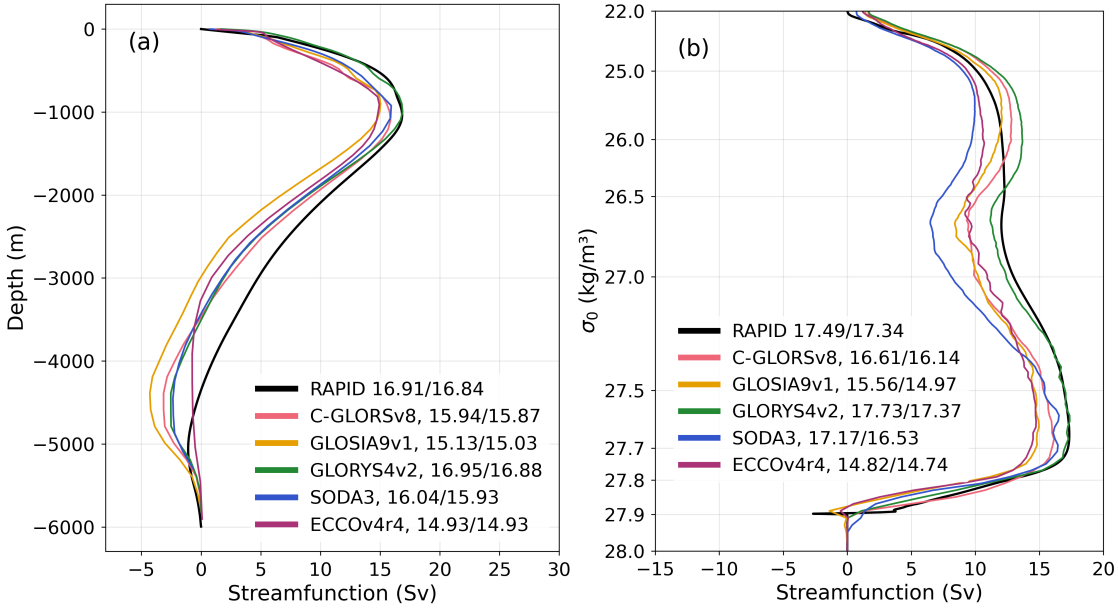



**Figure 2: Vertical profiles of time-mean AMOC overturning streamfunctions at the RAPID section in (a) depth and (b) $\sigma_0$ coordinates, over 04/2004 to 03/2023 except ECCOv4r4 from 04/2004 to 03/2017. Two values of AMOC strength in each inset are: mean peak-AMOC / peak mean-AMOC.**

https://doi.org/10.5194/egusphere-2026-6871
Preprint. Discussion started: 13 November 2026
© Author(s) 2026. CC BY 4.0 License.

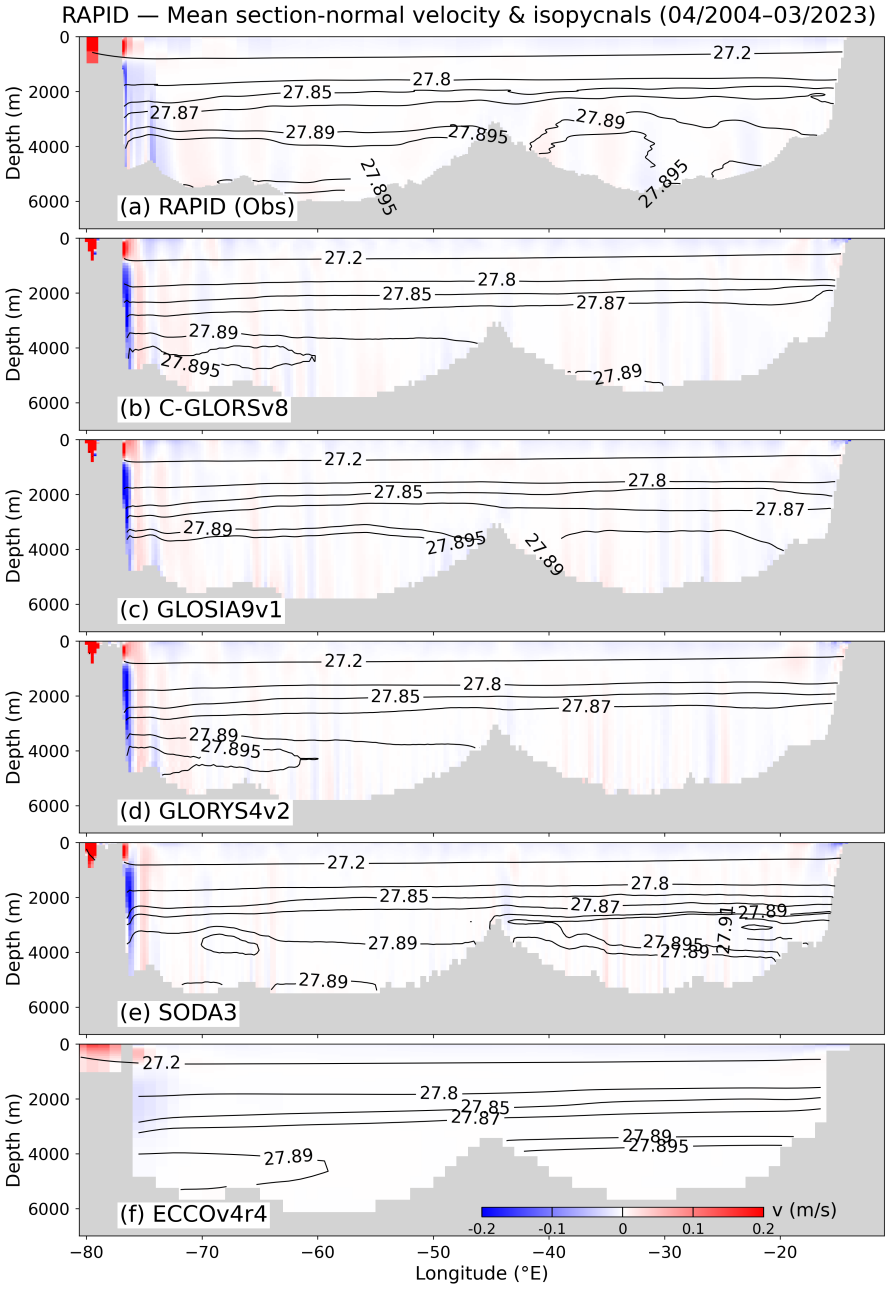



**Figure 3: Mean meridional velocity fields at the RAPID section along with contours of time-mean $\sigma_0$. Time-mean period 04/2004–03/2023 for RAPID and the reanalysis products, except ECCOv4r4 truncated at 03/2017. The velocity is shown on a linear scale (see colorbar). RAPID mooring locations are shown in McCarthy et al. (2015, Fig. 2.1).**

### 4.3 OSNAP AMOC comparisons

We next examine the vertical overturning structure at OSNAP: this section has only been monitored since 2014, so shorter time-mean periods are used (08/2014 to 07/2022).

https://doi.org/10.5194/egusphere-2026-6871
Preprint. Discussion started: 13 November 2026
© Author(s) 2026. CC BY 4.0 License.

Figure 4a shows the full OSNAP section, with Fig. 4b showing OSNAP East (of Greenland) and Fig. 4c showing OSNAP West across the Labrador Sea. Only overturning in $\sigma_0$ space is shown, because the depth-defined overturning is much weaker at this latitude (Fig. 1b). A surface reference is preferred in the streamfunction calculation, as in Lozier et al. (2019), because strong flows of dense water occur here in the upper ocean boundary currents. The full section overturning shows good agreement with observations. East and West contributions partly offset each other in the full-section total (see the along-track transports in Figs. S1 and S2 of the Supplement), and the overturning peak is narrower in the full section than in the East section alone. For the full section, the peak overturning strengths agree well for most products, at around 15–17 Sv, with the peak at about $\sigma_0$ = 27.6–27.7 kg m$^{-3}$ (27.6 kg m$^{-3}$ in the array); SODA3 transports are lower, ~12 Sv. ECCOv4r4 also has lower overturning in the East section, partly offset by higher overturning in the West section, suggesting additional water-mass transformation in the Labrador Sea. For both OSNAP observations and some reanalysis products, the mean peak-AMOC exceeds the peak mean-AMOC by about 1.5 Sv, more than at RAPID (Sect. 4.2), suggesting more significant variability in the peak overturning density (detail in Appendix A.3). The lower maximum densities of the southward flows compared to observations represent the main integrated biases among the reanalysis products, with no net southward transports denser than ~27.85 kg m$^{-3}$, whereas the OSNAP array shows substantial southward transport in these classes, extending to around 27.9 kg m$^{-3}$ (Fig. 4) in the eastern section. Most of this observed dense transport crosses the East section, where the products carry little or no net transport; across the West section, net transport at these densities is small in both the observations and the products (Figs. S1 and S2).

Figure 5 shows the comparison of mean cross-section normal velocity and density (contoured) across the OSNAP section. Agreement is good apart from in the densest part of the AMOC lower limb. Along the East Greenland slope, the observed isopycnals slope towards Greenland, whereas in the reanalyses they are flat or rise. The OSNAP array shows southward flow in these dense layers along the East Greenland slope and east of the Mid-Atlantic Ridge, which is absent in the reanalyses, where southward flow rarely reaches the bottom. This difference agrees with Winkelbauer et al. (2026) and is likely related to the limited reanalysis deep data constraints.

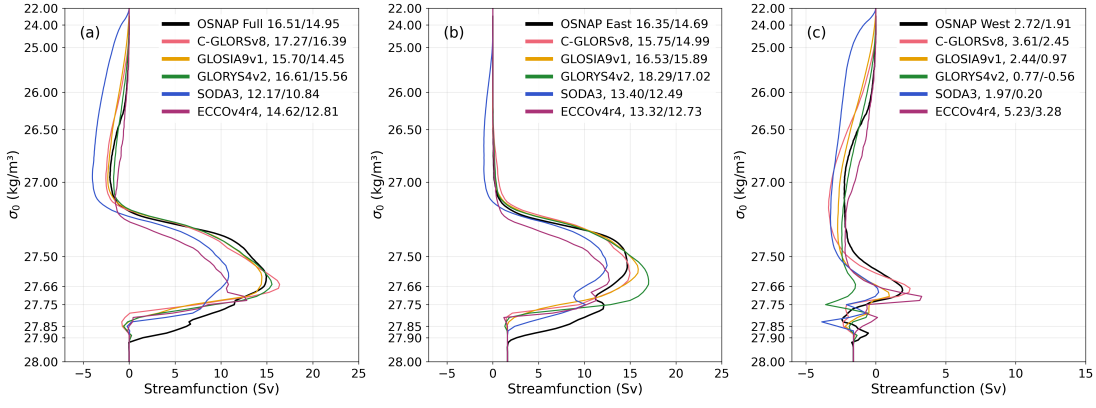
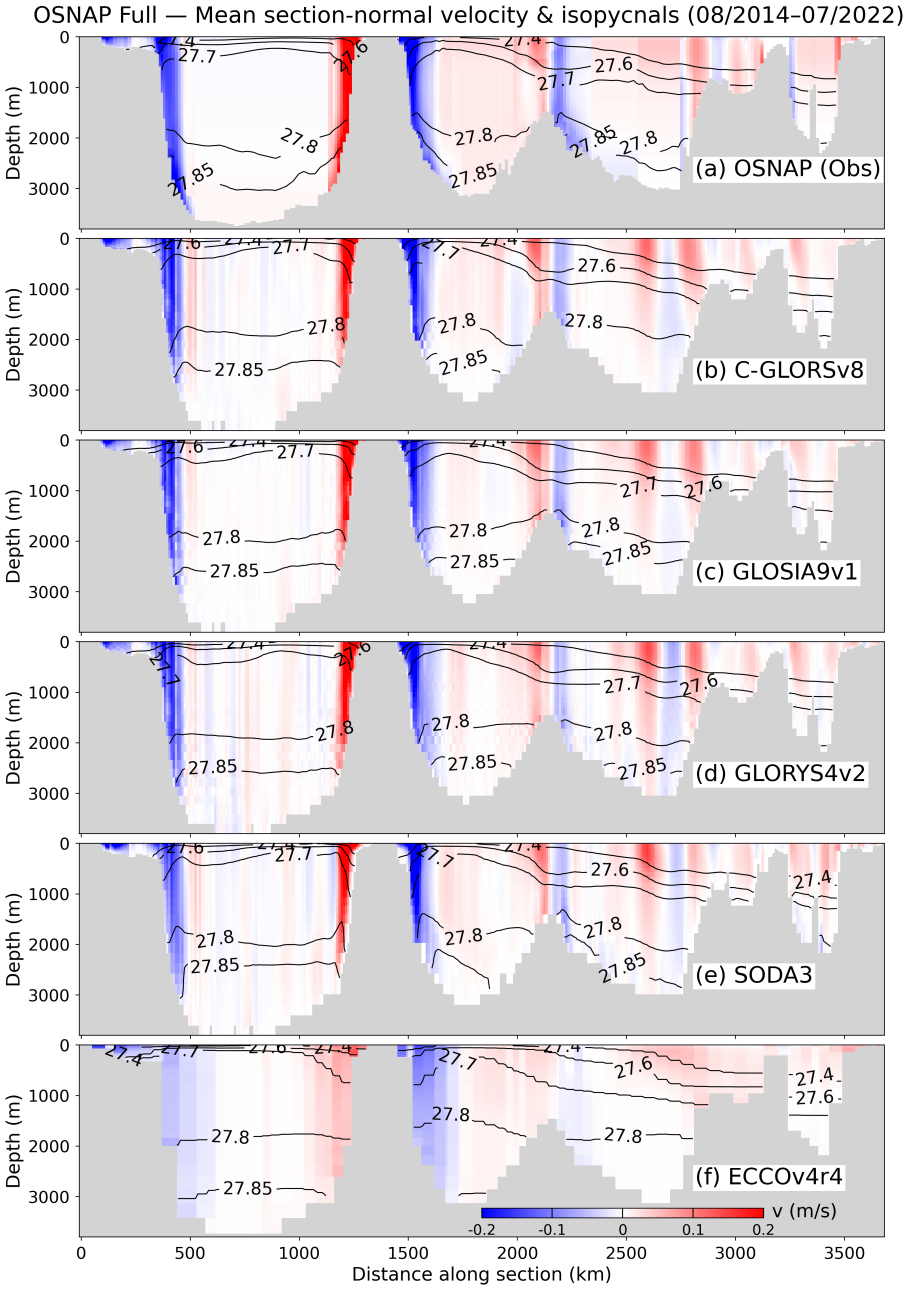



**Figure 4: Time-mean overturning profiles Ψ($\sigma_0$) for (a) OSNAP, (b) OSNAP East, and (c) OSNAP West sections, over 08/2014 to 07/2022 except ECCOv4r4 from 08/2014 to 07/2017. As in Fig. 2, the two inset values show the mean peak-AMOC, followed by the peak mean-AMOC, which corresponds to the streamfunction peaks in the figure.**

https://doi.org/10.5194/egusphere-2026-6871
Preprint. Discussion started: 13 November 2026
© Author(s) 2026. CC BY 4.0 License.




285

**Figure 5: Time-mean field of velocity and density section across OSNAP, averaged over 08/2014–07/2022, except ECCOv4r4 truncated at 07/2017. Velocity is normal to the OSNAP section and is shown on a linear scale, and the very small barotropic correction is not applied. OSNAP mooring locations are shown in Lozier et al. (2019, Fig. 2).**

### 4.4 SAMBA AMOC comparisons

290 The SAMBA section at 34.5°S in the South Atlantic connects the AMOC to the thermohaline circulation in the global ocean. Figure 6 shows the time-mean overturning profiles in depth (a) and $\sigma_0$ space (b) from the different reanalysis products,

https://doi.org/10.5194/egusphere-2026-6871
Preprint. Discussion started: 13 November 2026
© Author(s) 2026. CC BY 4.0 License.

averaged over 03/2009–04/2017. The overturning maximum is located at a greater depth, around 1500 m, and there are considerable differences in overturning strength between products. GLORYS4v2 has a strong 19.21 Sv time-mean peak overturning, while GLOSIA9v1 and ECCOv4r4 are 5–6 Sv lower, at 14.11 Sv and 13.04 Sv, respectively, with C-GLORSv8 (16.68 Sv) and SODA3 (16.48 Sv) in between, as could also be seen over a longer period in the streamfunction, Fig. 1b. The SAMBA section does not provide streamfunction analyses, only a reference mean upper-cell MOC (14.7 Sv, Meinen et al., 2018; dashed line in Fig. 6a), which lies within the range of the reanalyses. However, this mean is considered the least reliable part of the SAMBA results, because model estimates are used to supplement the observations (Weijer et al., 2020). Other observational estimates, covering different periods, are higher: about 18 Sv from XBT and Argo data (Dong et al., 2009; Garzoli et al., 2013) and 19.45 Sv from an altimetry-derived estimate (Dong et al., 2015). Most products show a weak reversed bottom cell below 3000 m (Fig. 6a) of ~1–2 Sv, strongest in GLOSIA9v1 and SODA3 and weakest in GLORYS4v2. In $\sigma_0$ space (Fig. 6b), the main NADW transports also have a considerably wider density range (27.5–27.8 kg m$^{-3}$) than in the Northern Hemisphere.

Figure 7 shows time-mean meridional velocity across the SAMBA section with mean $\sigma_0$ contours from the reanalyses, although these are not available from the observational analysis for comparison. There is good consistency between products for the major currents on both the western and eastern boundaries. ECCOv4r4 shows similar current systems, but at its coarser resolution it does not resolve the same complexity of the western boundary currents (Mignac et al., 2018).

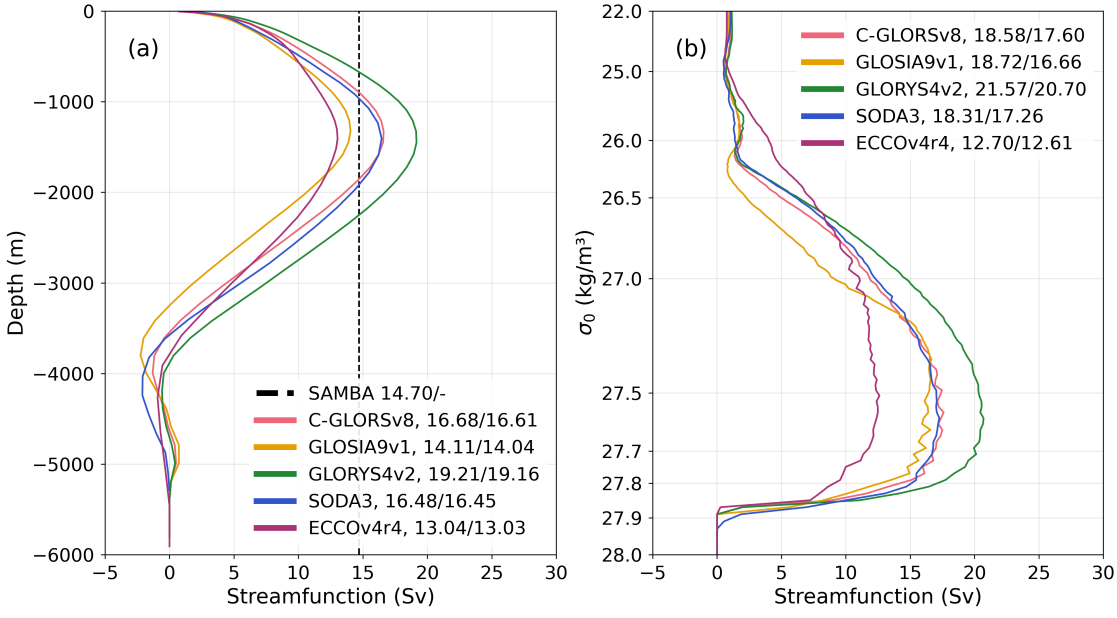
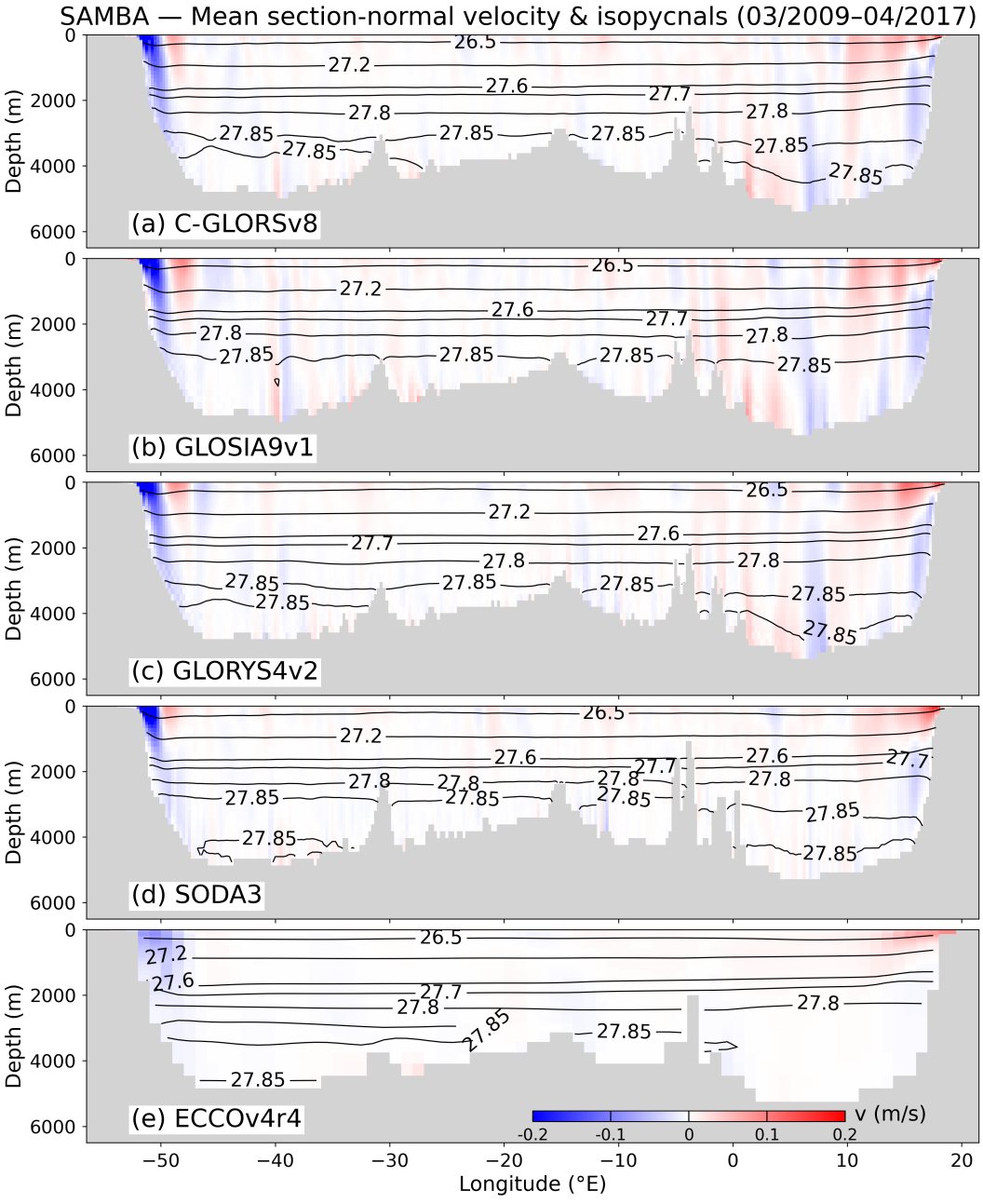



**Figure 6: SAMBA array location 34.5°S time-mean vertical transport profiles in (a) depth space and (b) $\sigma_0$ space, averaged over 03/2009–04/2017, the span of the SAMBA observational record, within which the observations themselves consist of two segments separated by a ~2.8-year gap. The array provides no vertical profile, so its entry in the legend of panel (a) carries only the reference mean upper-cell MOC of 14.7 Sv (black dashed line, Meinen et al., 2018). The two transport numbers in each inset are the mean peak-AMOC / peak mean-AMOC.**

https://doi.org/10.5194/egusphere-2026-6871
Preprint. Discussion started: 13 November 2026
© Author(s) 2026. CC BY 4.0 License.




315 **Figure 7: Time-mean field of meridional velocity and density section across SAMBA at 34.5°S, averaged over the same 03/2009–04/2017 window as Fig. 6. Velocity is normal to the SAMBA section and is shown on a linear scale.**

## 5. Transport variability, including trends

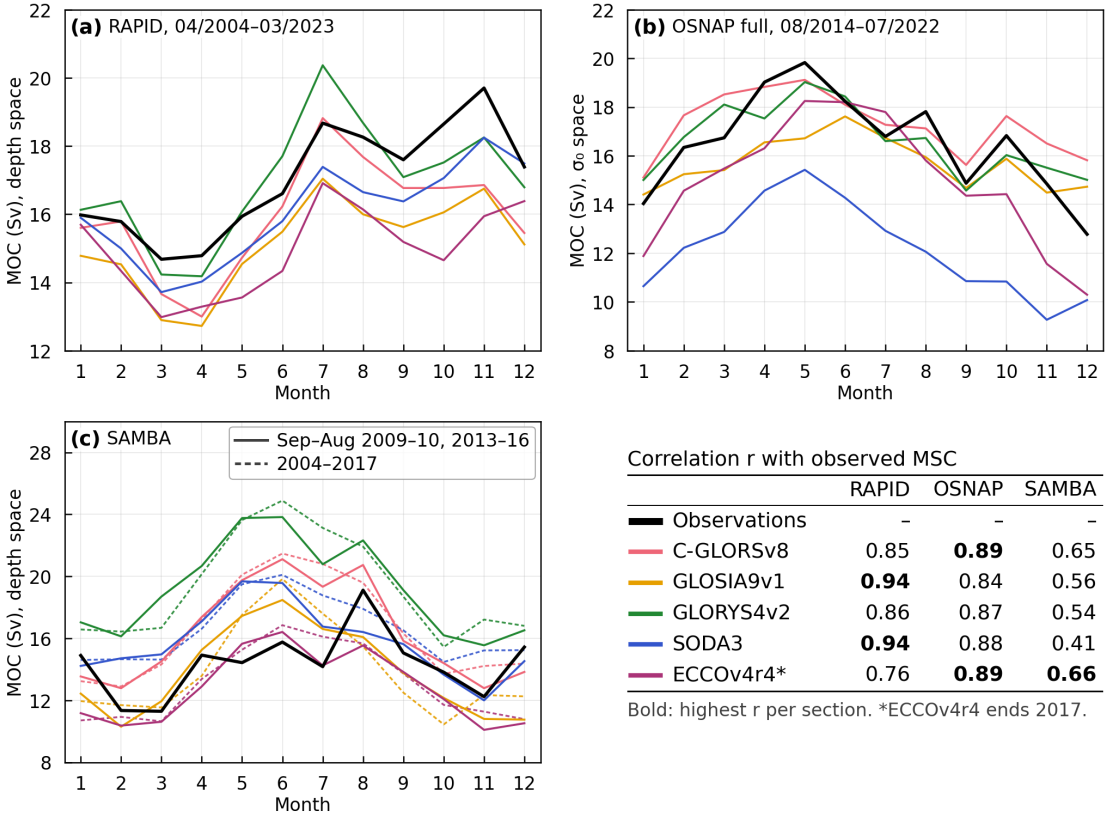
This section compares the seasonal cycle, deseasonalised variability, and longer-term tendencies of the AMOC at the three monitored sections.

https://doi.org/10.5194/egusphere-2026-6871
Preprint. Discussion started: 13 November 2026
© Author(s) 2026. CC BY 4.0 License.

### 5.1 Seasonal variability

Figure 8 shows the MSC of the AMOC at RAPID (a), OSNAP full (b), and SAMBA (c). Correlations with the observations (listed in the table in Fig. 8) are high in the North Atlantic (Fig. 8a, b) and lower in the south (Fig. 8c), probably because the SAMBA record is shorter, resulting in larger month-to-month variations. At OSNAP and SAMBA, much of the seasonal variability comes from the Ekman component (Fox et al., 2025; Pita et al., 2024), whereas at RAPID the geostrophic contributions are larger (Kanzow et al., 2010). The product MSCs have generally similar phases at each section, and much of the spread among them reflects offsets in mean transport (Sect. 4). At RAPID, the observed MSC has two maxima, in July and November, and the November maximum is larger, consistent with the autumn maximum reported by Kanzow et al. (2010). All products reproduce both maxima (the second falls in December in ECCOv4r4), but their relative amplitudes differ: in most products the July maximum is larger, and only SODA3 has the larger November maximum seen in the observational estimates. At SAMBA, the product MSCs are offset from one another by several Sv but share a similar shape, although with weaker peaks in August than observed. Dashed curves in Fig. 8c show each product's 2004–2017 MSC, spanning the estimated effective Argo observations to the end of ECCOv4r4. These MSCs have similar main phase and amplitude to the corresponding SAMBA-period MSCs, but with the August anomaly smoothed out and less month-to-month noise: the 4-yr SAMBA-period MSCs differ from them by 0.7–1.2 Sv RMS, as expected from sampling only four years.

https://doi.org/10.5194/egusphere-2026-6871
Preprint. Discussion started: 13 November 2026
© Author(s) 2026. CC BY 4.0 License.




Correlation r with observed MSC

| | RAPID | OSNAP | SAMBA |
|---|---|---|---|
| Observations | – | – | – |
| C-GLORSv8 | 0.85 | **0.89** | 0.65 |
| GLOSIA9v1 | **0.94** | 0.84 | 0.56 |
| GLORYS4v2 | 0.86 | 0.87 | 0.54 |
| SODA3 | **0.94** | 0.88 | 0.41 |
| ECCOv4r4* | 0.76 | **0.89** | **0.66** |

Bold: highest r per section. *ECCOv4r4 ends 2017.

**Figure 8: MSCs for the peak AMOC at each of the three monitored array sections (a) RAPID, (b) OSNAP full and (c) SAMBA. The OSNAP section is in σ₀ space while the others are in depth space. Black lines show the observed MSCs, computed over 04/2004–03/2023 (RAPID), 08/2014–07/2022 (OSNAP) and four complete September–August cycles (2009–2010 and 2013–2016; SAMBA); the solid reanalysis MSCs use the same months (ECCOv4r4 only up to 2017). The table (bottom right) lists the correlation r between each reanalysis MSC and the observed MSC at each section; bold marks the highest r per section. In panel (c), dashed lines show each product's seasonal cycle over the longer 2004–2017 window.**

### 5.2 RAPID transport time series

Figure 9a shows the RAPID monthly AMOC strength from 1993 onwards. Panel (b) shows deseasonalised monthly anomalies used for the model–observation comparison and associated statistics: correlation, RMSD, and std. Correlations with array variability range from SODA3 (r=0.63) to GLORYS4v2 (r=0.85). RMSDs of the monthly anomalies against RAPID observations range from GLORYS4v2 (1.55 Sv) to SODA3 (2.43 Sv), all substantially smaller than the RAPID anomaly std (2.82 Sv) over the blue-shaded MSC reference period. Two uncorrelated time series with similar standard deviations would be expected to have an RMSD of approximately √2 times their common standard deviation. This shows that all the products capture the observed interannual and higher-frequency variability well. All products show the clear AMOC minimum in early 2010 seen in the observations (Cunningham et al., 2013). Much of the other higher-frequency and lower-frequency variability is also consistent among products. Figure S3 of the Supplement shows the same series with a centred 12-month running mean, which makes the slower changes easier to see; it is not used for the statistics or trends.

https://doi.org/10.5194/egusphere-2026-6871
Preprint. Discussion started: 13 November 2026
© Author(s) 2026. CC BY 4.0 License.

Some of the high-frequency variability will be associated with Ekman transports, likely to be consistent through the same or similar atmospheric forcing. In Fig. S4 we show a similar plot to Fig. 9b in which the Ekman transport component from the RAPID array is also removed from each reanalysis time series. The remaining variability is still well correlated between products and with observations. We only do this for RAPID, which has a sufficiently long record. Panel (c) shows linear trends of the panel (b) anomalies over 1993–2022 and the decades 1993–2002, 2003–2012 and 2013–2022 (Appendix A.3), with error bars as ±2 standard errors, which assume independent residuals and may therefore underestimate the uncertainty. Trends are discussed in Sect. 5.5.

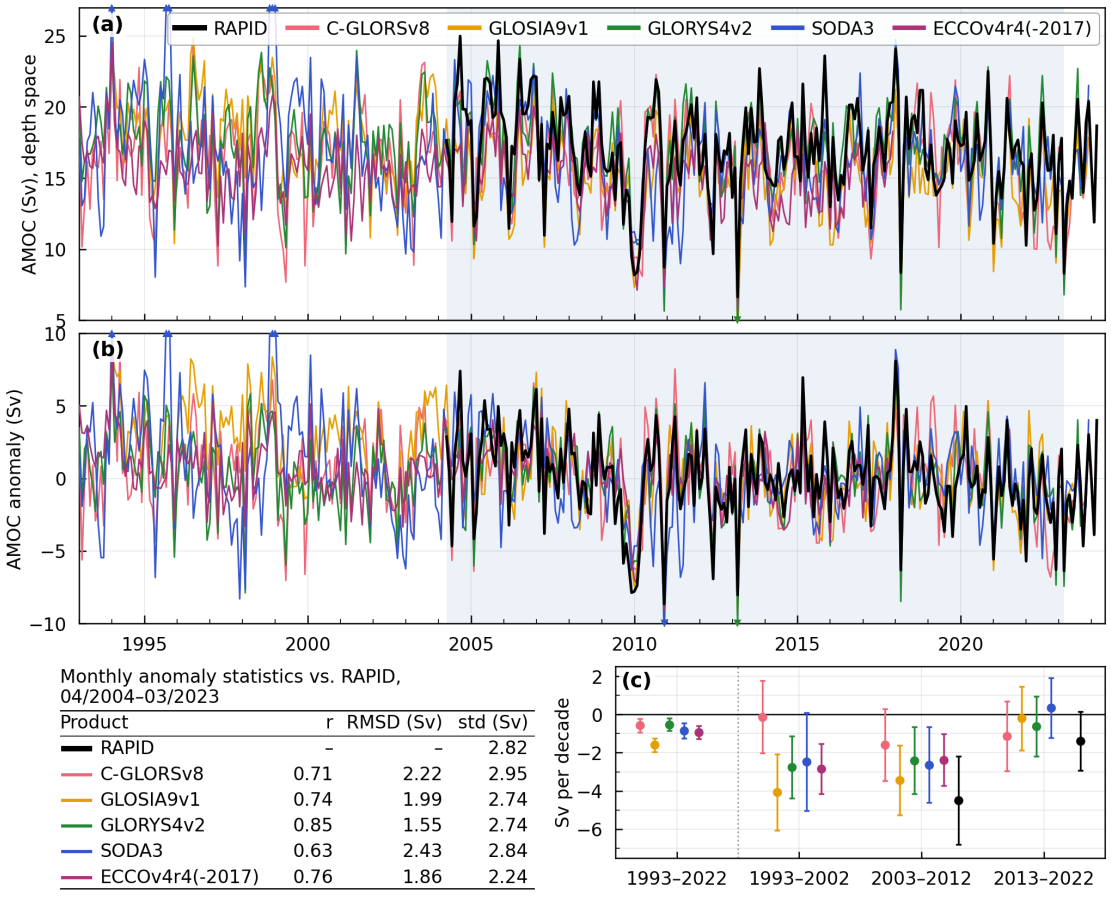



**Figure 9: Full time series of AMOC comparison at the RAPID section, over 1993–2023. (a) Raw monthly AMOC in depth space. (b) Monthly AMOC anomalies after removal of the MSC. (c) Linear trends of the panel (b) anomalies; error bars are ±2 standard errors. Blue shading indicates the reference period for the MSC and statistics calculation (04/2004–03/2023); the bottom-left table gives the correlation (r), RMSD and std of the panel (b) anomalies for each reanalysis against the observations over this period (ECCOv4r4 to 12/2017). Values outside the axis range in (a) and (b) are marked by triangles.**

### 5.3 OSNAP transport time series

Figure 10 shows the OSNAP full AMOC (a) and the AMOC anomalies with the MSC removed (b), from 1993 onwards, including the 20 years prior to the availability of OSNAP array data. In Fig. 10a the significantly lower transports in

https://doi.org/10.5194/egusphere-2026-6871
Preprint. Discussion started: 13 November 2026
© Author(s) 2026. CC BY 4.0 License.

ECCOv4r4 are clearly seen, apart from during a brief period in the early 2000s, which ends by 2017. The strong decline of SODA3 during the first two decades also stands out. In Fig. 10b the anomalies show a considerable degree of higher-frequency agreement between products throughout the time series, with occasional exceptions. During the monitored period, correlations with OSNAP range from GLOSIA9v1 (r=0.26) to GLORYS4v2 (r=0.58), and RMSDs to OSNAP anomalies range from GLOSIA9v1 (3.07 Sv) to GLORYS4v2 (2.29 Sv). With the observed OSNAP anomaly population std of 2.63 Sv, an uncorrelated time series of similar amplitude would be expected to have an RMSD ~3.7 Sv, so all these reanalysis products are again capturing substantial observed AMOC variability, although less well than at the RAPID section. Panel (c) shows the linear trends of the panel (b) anomalies, discussed in Sect. 5.5.

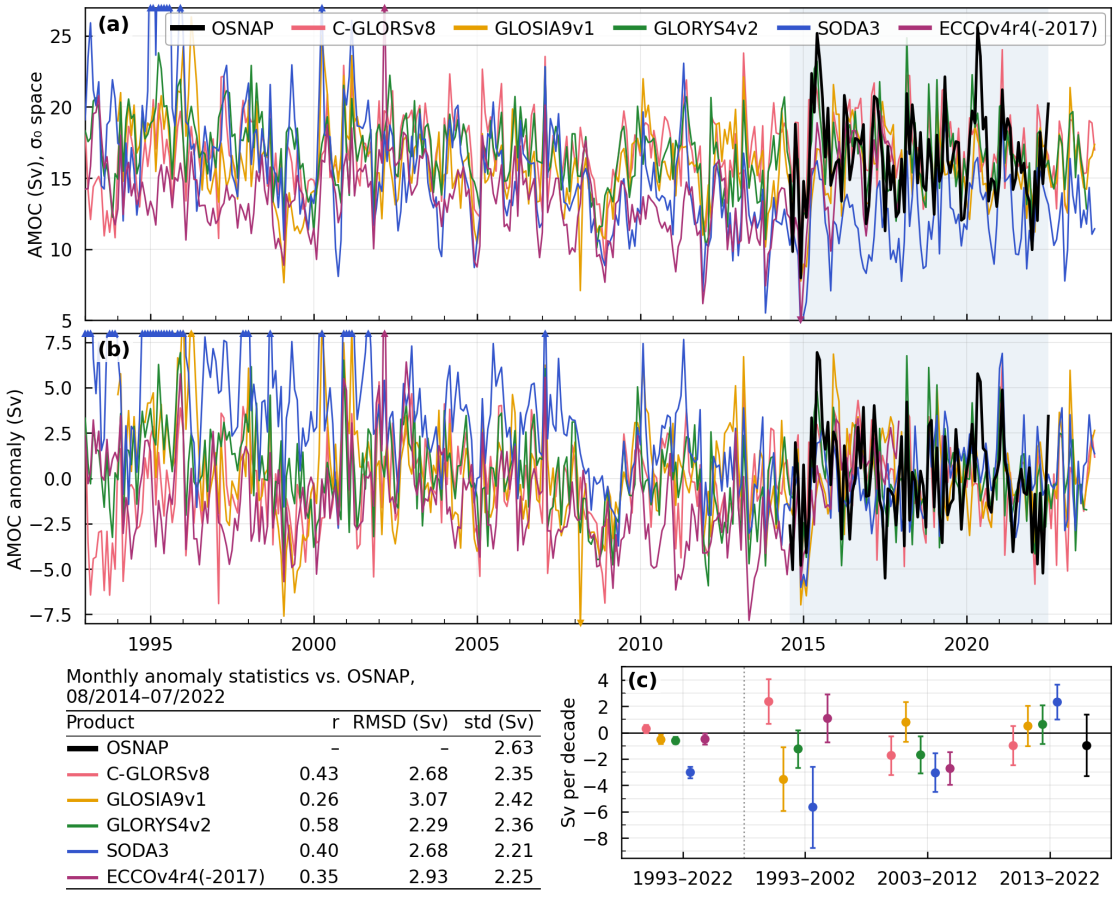



**Figure 10: Full time series of AMOC comparison at the OSNAP section. (a) Raw monthly AMOC in σ₀ space. (b) Monthly AMOC anomalies after removal of the MSC. (c) Linear trends of the panel (b) anomalies, as in Fig. 9c; the OSNAP observed trend is fitted over 08/2014–07/2022 only. Blue shading indicates the observational reference period (08/2014–07/2022); the bottom-left table gives the correlation (r), RMSD and std of the panel (b) anomalies over matched valid months (ECCOv4r4 to 12/2017). Values outside the axis range in (a) and (b) are marked by triangles.**

https://doi.org/10.5194/egusphere-2026-6871
Preprint. Discussion started: 13 November 2026
© Author(s) 2026. CC BY 4.0 License.

### 5.4 SAMBA transport time series

Figure 11 shows the SAMBA AMOC (a) and the AMOC anomalies with the MSC removed (b) from 1993 onwards. Blue shading marks the two observational-availability segments used for the time-series comparison. The observed MSC is a harmonic fit to the four complete September–August cycles within those segments, and each reanalysis MSC is taken from 2004–2017 (dashed curves in Fig. 8c; Appendix A.3). Panel (b) compares each reanalysis directly with SAMBA over all months with overlapping valid observations: correlations range from 0.05 to 0.29, RMSDs from 5.13 to 5.69 Sv, and reanalysis anomaly std from 1.77 to 2.79 Sv, against an observed anomaly std of 5.22 Sv. Panel (c) shows the linear trends of the reanalysis anomalies in panel (b), discussed in Sect. 5.5.

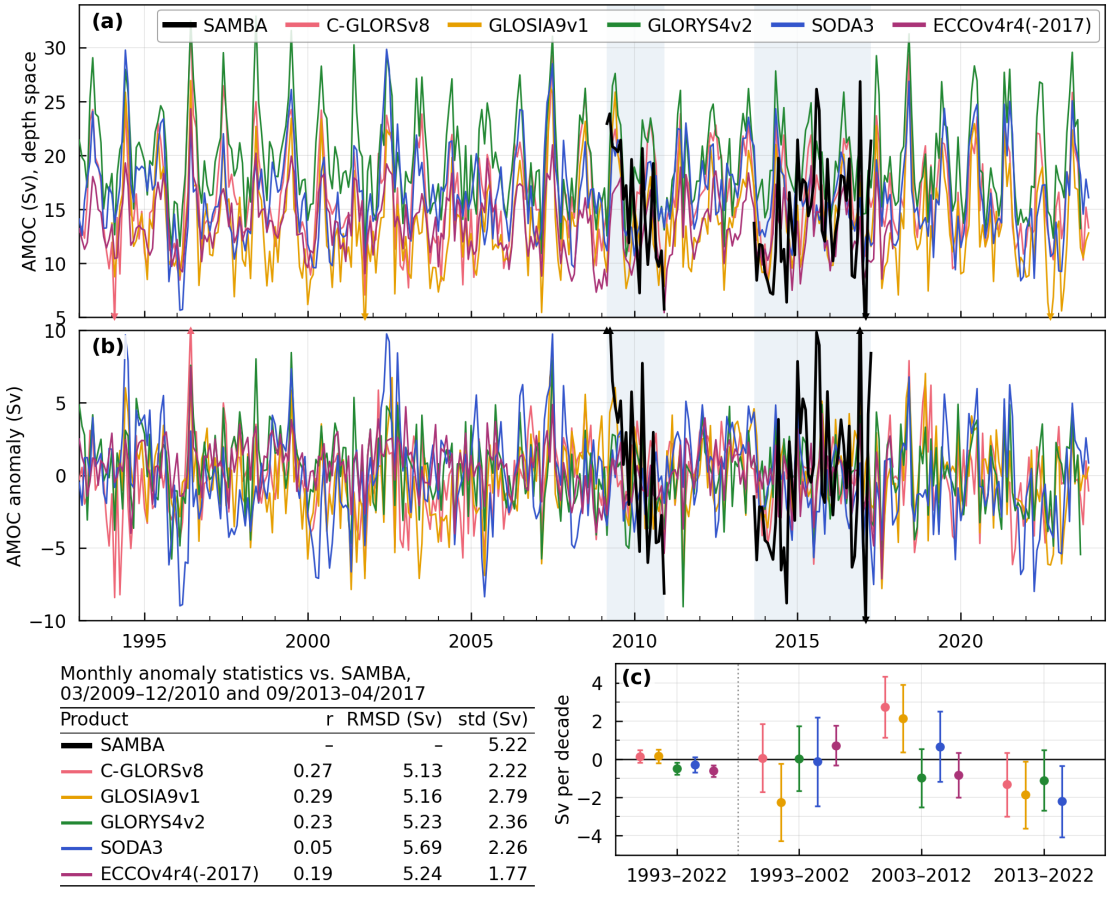



**Figure 11: Full time series of AMOC comparison at the SAMBA section. (a) Raw monthly AMOC in depth space. (b) Monthly AMOC anomalies after removal of the MSC. (c) Linear trends of the panel (b) anomalies, as in Fig. 9c; no SAMBA observed trend is shown. Blue shading marks the observed segments used for the model–observation statistics, which are calculated from matched valid months; the bottom-left table gives the correlation (r), RMSD and std of the panel (b) anomalies. Values outside the axis range in (a) and (b) are marked by triangles.**

https://doi.org/10.5194/egusphere-2026-6871
Preprint. Discussion started: 13 November 2026
© Author(s) 2026. CC BY 4.0 License.

Although direct agreement with SAMBA observations is weak over the short, discontinuous record, the reanalyses retain moderate internal temporal consistency over their longer pairwise overlaps; the reanalysis-only comparison is provided in Fig. S5 of the Supplement.

### 5.5 Longer-term tendencies across the three sections

Figures 9c, 10c and 11c show the whole-period (1993–2022) and decadal trends of the panel (b) anomalies (Appendix A.3). At RAPID, Fig. 9c, the three products with complete records (C-GLORSv8, GLORYS4v2, SODA3) display a long-term weakening of −0.5 to −0.8 Sv per decade over 1993–2022, and GLOSIA9v1 (starting in 1994) shows a larger decline; however, the fitted trends differ substantially between decades. Products generally agree with the array on a downward trend in 2003–2012, and no significant trend in 2013–2022. In 1993–2002, three products have a significant negative trend and two do not, but caution is required over how these different products are initialised and then respond to the sudden introduction of altimetry in 1993.

There is little agreement on trends between the products at OSNAP. SODA3's negative long-term trend is a strong outlier, and fitted trends over the most recent decade differ in sign among products; earlier decades likewise show no consensus. At SAMBA, no consistent long-term tendency is identified across the reanalyses. RAPID is therefore the only section where the products share a long-term tendency, primarily due to the well reproduced decline 2003–2012.

## 6. Discussion and Conclusions

We have evaluated the representation of the Atlantic Meridional Overturning Circulation in five current-generation ocean reanalyses against observations from the RAPID, OSNAP and SAMBA monitoring arrays. The comparison considers both the time-mean overturning structure and its temporal variability, using depth or density coordinates as appropriate for each section. Table 3 summarises the main findings from the three monitored sections.

**Table 3: Summary of the main AMOC findings at the RAPID, OSNAP and SAMBA monitoring sections.**

| Finding | RAPID | OSNAP | SAMBA |
|---|---|---|---|
| **Mean upper-cell AMOC** | Generally close agreement, with most products slightly weaker than the array estimate | Generally close agreement for the NEMO-based products; SODA3 and ECCOv4r4 are weaker | Large inter-reanalysis spread |
| **Deep / overturning structure** | Stronger abyssal cells and differences in the deep return flow; the deepest southward transport occurs at slightly lower density than in the array estimate | Deep southward transport occurs systematically at lower densities than in the array estimate; East and West contributions partly offset each other in the full-section total | No full observed overturning/velocity structure is available for an equivalent comparison |

https://doi.org/10.5194/egusphere-2026-6871
Preprint. Discussion started: 13 November 2026
© Author(s) 2026. CC BY 4.0 License.

| Finding | RAPID | OSNAP | SAMBA |
|---|---|---|---|
| **Deseasonalised variability** | Strong agreement; the 2010 minimum and much of the interannual variability are reproduced | Moderate agreement, clearly weaker than at RAPID | Weak direct agreement; short and discontinuous observations limit the assessment |
| **Long-term tendency** | Weak long-term decline across reanalyses, primarily focussed on the well-monitored 2003–2012 period of decline | No consistent cross-product trend | No consistent cross-product trend |

Seasonal cycles are generally reproduced at all three sections, although common atmospheric forcing, particularly Ekman variability, contributes to this agreement.

The mean upper-cell overturning at RAPID and OSNAP is generally in relatively close agreement with the array estimates. This agreement does not extend equally to the deeper overturning structure. At RAPID, the reanalyses show stronger reversed abyssal cells than the array inversion and differences in the depth of the southward return flow. The deepest southward transports occur at lower densities than in the corresponding array estimates, with the largest OSNAP differences occurring in the eastern part of the section. These comparisons therefore show that agreement in integrated upper-cell transport does not necessarily imply similarly close agreement in the deeper density and velocity structure. Deep-ocean observational constraints on the reanalyses remain limited, while assumptions in the array inversions may also contribute to some of the model–array differences; their relative contributions cannot be separated here.

The temporal comparison shows a clear contrast between RAPID and OSNAP. Deseasonalised AMOC variability is reproduced well at RAPID, including the pronounced minimum in early 2010 and much of the observed interannual variability, whereas agreement with OSNAP is more moderate. Figure 12 groups the RAPID and OSNAP deseasonalised anomaly comparisons among reanalyses into a Taylor diagram. Most products have normalised standard deviations between 0.75 and 1, slightly lower than observed. The RAPID points generally show higher correlations and lower centred RMS differences than the OSNAP points, although all the products have some significant skill in reproducing OSNAP variability. GLORYS4v2 has the highest correlation and lowest RMSD at both sections, while SODA3 has the lowest correlation at RAPID and GLOSIA9v1 the lowest at OSNAP. Note that observational errors cannot be quantified at OSNAP because no error budget is available (Sect. 2.2.2). SAMBA is not included because its record is short and discontinuous.

https://doi.org/10.5194/egusphere-2026-6871
Preprint. Discussion started: 13 November 2026
© Author(s) 2026. CC BY 4.0 License.

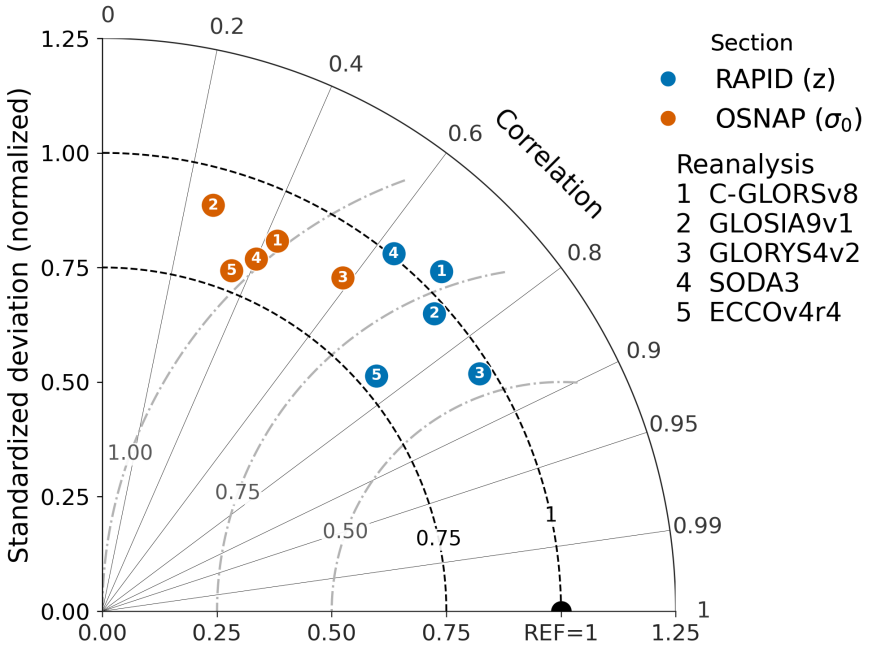



**Figure 12: Taylor-diagram synthesis of deseasonalised AMOC anomaly agreement at RAPID (26.5°N, depth space) and OSNAP (≈57°N, σ₀ space). Products spanning the full observation-reference periods used in Figs. 9b and 10b (04/2004–03/2023 for RAPID; 08/2014–07/2022 for OSNAP) use those same periods; products that do not span the full reference period are retained using their shorter available paired overlap. For every marker, correlation, model and observation standard deviation, and CRMSD are calculated from the same paired months.**

South Atlantic comparisons are less conclusive. The reanalyses show substantially greater spread in mean upper-cell transport at SAMBA, while the available observational record is short, discontinuous and sensitive to the definition of the diagnosed overturning (Sect. 2.2.3). There is some consistency in variability between reanalysis products, at seasonal and interannual timescales, but apart from superficial seasonal variations, the present comparison cannot match AMOC variability here with observations due to the large uncertainties.

The analysis identified weak negative long-term AMOC trends shared by all the reanalyses at RAPID, although these are only consistent on decadal timescales due to the well-observed downward trends in 2003–2012, with RAPID trends being less consistent in other decades, and no consistent trends could be identified at other sections in the 30-year time series available. The first decade of these products may also be affected by initialisation differences, and the OLS standard errors used here may also underestimate trend uncertainty because of autocorrelation (Santer et al., 2000), so we would not interpret current results as supporting long-term AMOC decline (Sect. 5.5).

Overall, the results show that current reanalyses agree well with observations in representing important aspects of AMOC variability, particularly the upper-cell variability at RAPID but also less robustly at OSNAP, while larger uncertainties remain in the deeper overturning structure, and in the South Atlantic. The close agreement in RAPID upper-cell variability

https://doi.org/10.5194/egusphere-2026-6871
Preprint. Discussion started: 13 November 2026
© Author(s) 2026. CC BY 4.0 License.

supports the use of reanalyses for monitoring this component of the AMOC and motivates reanalysis use as candidate ocean initial states for coupled decadal predictions.

## Appendix A: Observational data, transport calculations and diagnostic details

### A.1 Observational products and error estimates

Reanalysis monthly means are used directly, higher-frequency RAPID and SAMBA observations are averaged to monthly values, and OSNAP is supplied natively as monthly means. Observational error has a random part, which averages to zero over time and affects the anomaly statistics, and a bias, which stays constant, affects the time mean and is removed with the seasonal cycle (Meinen et al., 2013). The published estimates (Table 2) are not propagated into the statistics, so the RMSDs and CRMSDs reported here include observational error.

The RAPID overturning transport is derived at twice-daily resolution with a 10-day low-pass filter applied; the density-space products and the depth–longitude section fields are provided at 10-day resolution. For RAPID, the RMS errors of McCarthy et al. (2015) include both random and bias-like parts.

The OSNAP streamfunction data have 481 density levels ($\sigma_0 \approx 23.3$–$28.1$ kg m$^{-3}$ at 0.01 kg m$^{-3}$ intervals) across the full OSNAP section, OSNAP East and OSNAP West; the gridded data give monthly cross-section normal velocity, temperature and salinity across the section. The OSNAP release also gives a Monte-Carlo uncertainty for each month (Lozier et al., 2019). We do not use it as an observational error, because it mainly reflects how much the input fields vary within each 30-day period rather than measurement error (Li et al., 2017; Lozier et al., 2019). Li et al. (2017) sampled a ¼° model (1990–2004) at the instrument positions and compared the resulting overturning maximum with the model's own: the 30-day RMS differences are 1.38 Sv (East) and 0.72 Sv (West), and the mean differences are −1.92 Sv and +0.13 Sv. These OSSE-based estimates differ in kind from the RAPID and SAMBA observational error estimates. The OSSE includes no instrument error, so the RMS differences quantify differences between the model-sampled and full-model overturning, rather than establishing a lower bound on the real array's monthly random error. The mean differences are signed estimates of the bias rather than bounds; using them assumes that the real array has the same bias as in this model run. If the East and West OSSE differences are independent, their quadrature sum is $\sqrt{(1.38^2 + 0.72^2)} \approx 1.56$ Sv.

Kersalé et al. (2020), using the basin-wide array, provide gap-free daily anomalies of upper-cell and abyssal-cell transports from 11 September 2013 to 16 July 2017, relative to reference means of 17.3 Sv (upper cell) and 7.8 Sv (abyssal cell). Fixed pressure interfaces are used: 1315 dbar for the upper cell MOC and 3155–4295 dbar for the abyssal cell MOC. The two products overlap from 11 September 2013 to 29 April 2017.

For SAMBA, the errors of Meinen et al. (2013, 2018) are too large to be useful here: the time scale of the random error is not given, so it cannot be converted to a monthly value, and it already exceeds the observed monthly anomaly standard deviation.

https://doi.org/10.5194/egusphere-2026-6871
Preprint. Discussion started: 13 November 2026
© Author(s) 2026. CC BY 4.0 License.

### A.2 Transport calculation

For the NEMO-based products, CDFTOOLS (MEOM Group, 2026) and StraitFlux (Winkelbauer et al., 2024) produced identical transports in our comparison; StraitFlux was used for most calculations because it facilitates specification of sections such as OSNAP. The reanalyses based on tripolar Arakawa grid layout are processed by StraitFlux. The ECCOv4r4 model uses a more complex grid representation – a lat-lon-cap (LLC) grid – so the native ECCO tools were used for AMOC assessments (ECCO Consortium, 2026). The OSNAP barotropic correction is applied during post-processing (Appendix A.3).

The StraitFlux line-integration approach represents each section as a stair-step path along model grid-cell faces and computes the transport from the native face-normal velocity components (u on zonal-facing and v on meridional-facing faces) multiplied by the face width and thickness. For the NEMO model, the U- and V-face thicknesses of the model mesh are used, so partial bottom cells are represented; for SODA3, which uses an Arakawa-B grid, StraitFlux first transforms the velocities to the tracer-cell faces of the C-grid, accounting for the cell dimensions and thicknesses. Temperature and salinity are averaged from the two adjacent tracer points onto each face before $\sigma_0$ is computed.

For ECCOv4r4, the ECCO tools select the native LLC cell faces, and transports are computed from UVELMASS and VVELMASS, which include the partial-cell fraction, multiplied by the face width and layer thickness.

### A.3 Diagnostic details

For the overturning streamfunction calculations and the RAPID/SAMBA comparison, the calculations accumulate the depth and $\sigma_0$ streamfunctions from bottom upward, or from high to low density, respectively, with the streamfunction referenced to zero at the bottom or the highest density class. Following the observational convention at OSNAP (Lozier et al., 2019), the $\sigma_0$-space overturning is instead accumulated from light to dense classes, with the streamfunction referenced to zero at the lightest density class. A uniform barotropic adjustment is applied to the cross-section normal velocity before this calculation to impose the OSNAP west- and east-arm transport targets (constant −1.6 and +1.6 Sv, respectively; Lozier et al., 2019). No barotropic constraint is applied at RAPID or SAMBA. The $\sigma_0$ transport values are calculated for each model grid-cell and assigned to constant 0.02 kg $m^{-3}$ bins (transport anomalies appear with larger bin sizes, e.g., Evans et al., 2023; Danabasoglu et al., 2026). To test the sensitivity to this choice, the full-section OSNAP and SAMBA $\sigma_0$ streamfunctions of C-GLORSv8, GLORYS4v2, GLOSIA9v1 and SODA3 were recalculated with bin widths of 0.005, 0.01, 0.015 and 0.02 kg $m^{-3}$. At every bin width, the time-mean peak AMOC exceeds the peak of the time-mean streamfunction (the two inset values in Figs. 4a and 6b), by 0.88–2.46 Sv. The peak of the time-mean streamfunction changes by less than 0.06 Sv across bin widths, whereas the time-mean peak AMOC decreases as the bins widen; the difference between the two values therefore decreases in every case, by 0.16–0.39 Sv (12–28 %) from 0.005 to 0.02 kg $m^{-3}$. At all bin widths, the difference is largest for GLOSIA9v1 at SAMBA and for SODA3 at OSNAP.

https://doi.org/10.5194/egusphere-2026-6871
Preprint. Discussion started: 13 November 2026
© Author(s) 2026. CC BY 4.0 License.

For each section, AMOC strength is searched over all depth levels in depth space; in $\sigma_0$ space, it is searched over density bins $\sigma_0 \geq 26.5$ kg m$^{-3}$ for RAPID and SAMBA, and 27–28 kg m$^{-3}$ for OSNAP sections. These searches select the upper-cell maximum over the analysed records, without an additional upper-coordinate cutoff.

The SAMBA MSC uses only the four complete September–August cycles within the two SAMBA observational segments (2009–2010 and 2013–2016; 48 months); however, four years are too short for stable monthly means, so the observed anomalies are taken relative to a fit of the mean plus annual and semi-annual harmonics to these 48 months, and the reanalysis anomalies relative to each product's 2004–2017 MSC.

Trend Analysis: The long-term AMOC trends are estimated by fitting the monthly AMOC strength anomalies using linear regression with ordinary least squares (OLS). Complete years are always used for each fitted period (where a reanalysis ends within a decade window, the trend is fitted over its available complete years). Trend uncertainties are the standard errors of the fitted slopes. Both slopes and standard errors are then converted into Sv per decade. Because monthly AMOC anomalies are strongly autocorrelated, these conventional regression standard errors, which assume independent residuals, may underestimate trend uncertainty. Trends are therefore interpreted descriptively rather than as formal significance tests. The fitted trends are shown in Figs. 9c, 10c and 11c, with error bars of ±2 standard errors. Where a record does not cover a full window, the available months are used: the RAPID observations from 04/2004 in 2003–2012, the OSNAP observations over 08/2014–07/2022, GLOSIA9v1 from 01/1994 in 1993–2022 and 1993–2002, and ECCOv4r4 to 12/2017 in 1993–2022; ECCOv4r4 is not fitted for 2013–2022, and the SAMBA observation record is too short for a meaningful trend estimate.

## Code and data availability

Reanalyses. Monthly velocity, temperature and salinity fields of the five reanalyses (Table 1) were obtained as follows: C-GLORSv8 from CMCC, GLORYS4v2 from Mercator Ocean International (Bourdallé-Badie et al., 2026) and GLOSIA9v1 from the UK Met Office; SODA3.15.2 (Carton et al., 2018) from the University of Maryland (https://www.soda.umd.edu/soda3/); and ECCOv4r4 from the NASA PO.DAAC (ECCO Consortium, 2021b; monthly three-dimensional volume fluxes, ECCO Consortium, 2021a, https://doi.org/10.5067/ECL5M-3VF44, and monthly temperature and salinity, ECCO Consortium, 2021c, https://doi.org/10.5067/ECL5M-OTS44, both on the llc90 grid).

Observations. RAPID-MOCHA-WBTS v2024.1a is available from the British Oceanographic Data Centre (Moat et al., 2026, https://doi.org/10.5285/48d0bf43-0598-ceb2-e063-7086abc062f1). The OSNAP May 2025 release, "Meridional Overturning Circulation Observed by the OSNAP Array from August 2014 to July 2022" (Fu et al., 2025b), is available from the Georgia Tech Digital Repository (https://doi.org/10.35090/gatech/78023). The SAMBA 34.5°S MOC time series (Meinen et al., 2018) is available from the SAMOC International page hosted by NOAA/AOML (https://www.aoml.noaa.gov/phod/SAMOC_international/).

https://doi.org/10.5194/egusphere-2026-6871
Preprint. Discussion started: 13 November 2026
© Author(s) 2026. CC BY 4.0 License.

Code. Transports were computed with CDFTOOLS (MEOM Group, 2026, https://github.com/meom-group/CDFTOOLS); with StraitFlux (Winkelbauer et al., 2024), using a modified version of release 1.1.0; and, for ECCOv4r4, with the ecco_v4_py package (ECCO Consortium, 2026).

## Author contributions

**Sukun Cheng:** Conceptualization, Methodology, Programming, Formal Analysis, Investigation, Data Curation, Writing – Original Draft, Writing – Review & Editing, Visualization. **Keith Haines:** Conceptualization, Supervision, Funding Acquisition, Original Draft, Writing – Review & Editing, Validation, Project Administration. **Susanna Winkelbauer:** Methodology (StraitFlux code provision), Data Curation, Discussion, Review. **Julia Araujo, Magdalena Balmaseda, Romain Bourdallé-Badie, Yumeng Chen, Gaël Forget, Doroteaciro Iovino, Chunxue Yang:** Project participation, Review.

## Competing interests

At least one of the co-authors serves as editor for the special issue to which this paper belongs.

## Acknowledgements

We thank Marie Drévillon, Andrea Cipollone, Richard Renshaw, Matthew Martin, and James A. Carton for providing reanalysis data and information on the products. Data from RAPID AMOC observing project is funded by the Natural Environment Research Council, U.S. National Science Foundation (NSF) with support from NOAA. They are freely available from https://rapid.ac.uk/. OSNAP data were collected and made freely available by the OSNAP (Overturning in the Subpolar North Atlantic Program) project and all the national programs that contribute to it (www.o-snap.org). The authors used Claude (Anthropic) and Codex (OpenAI) for the purpose of language editing, grammatical refinement, and code for figure adjustments. The manuscript text was written by the authors, and all analyses, results and interpretations are the authors' own; the authors reviewed and verified all AI-assisted output and take full responsibility for the content of the manuscript.

## Financial support

This research has been supported by the Copernicus Marine Environment Monitoring Service (contract no. 24254L03-COP-GLORAN-MER IP-4000), which funded S. Cheng, K. Haines and Y. Chen. S. Cheng and K. Haines are also supported by the UK Natural Environment Research Council (NERC) through the National Centre for Earth Observation (NCEO)

https://doi.org/10.5194/egusphere-2026-6871
Preprint. Discussion started: 13 November 2026
© Author(s) 2026. CC BY 4.0 License.

575 International Programme (contract no. PR140015; grant no. NE/X006328/1), and Y. Chen by NERC NCEO (contract no. PR140015; grant no. NE/Y006216/1).

## References

Baker, J. A., Renshaw, R., Jackson, L. C., Dubois, C., Iovino, D., Zuo, H., Perez, R. C., Dong, S., Kersalé, M., Mayer, M., Mayer, J., Speich, S., and Lamont, T.: South Atlantic overturning and heat transport variations in ocean reanalyses and 580 observation-based estimates, in: 7th edition of the Copernicus Ocean State Report (OSR7), edited by: von Schuckmann, K., Moreira, L., Le Traon, P.-Y., Grégoire, M., Marcos, M., Staneva, J., Brasseur, P., Garric, G., Lionello, P., Karstensen, J., and Neukermans, G., Copernicus Publications, State Planet, 1-osr7, 4, https://doi.org/10.5194/sp-1-osr7-4-2023, 2023.

Balmaseda, M. A., Hernandez, F., Storto, A., Palmer, M. D., Alves, O., Shi, L., Smith, G. C., Toyoda, T., Valdivieso, M., Barnier, B., Behringer, D., Boyer, T., Chang, Y.-S., Chepurin, G. A., Ferry, N., Forget, G., Fujii, Y., Good, S., Guinehut, S., 585 Haines, K., Ishikawa, Y., Keeley, S., Köhl, A., Lee, T., Martin, M. J., Masina, S., Masuda, S., Meyssignac, B., Mogensen, K., Parent, L., Peterson, K. A., Tang, Y. M., Yin, Y., Vernieres, G., Wang, X., Waters, J., Wedd, R., Wang, O., Xue, Y., Chevallier, M., Lemieux, J.-F., Dupont, F., Kuragano, T., Kamachi, M., Awaji, T., Caltabiano, A., Wilmer-Becker, K., and Gaillard, F.: The Ocean Reanalyses Intercomparison Project (ORA-IP), J. Oper. Oceanogr., 8, S80–S97, https://doi.org/10.1080/1755876X.2015.1022329, 2015.

590 Bellomo, K., Angeloni, M., Corti, S., and von Hardenberg, J.: Future climate change shaped by inter-model differences in Atlantic meridional overturning circulation response, Nat. Commun., 12, 3659, https://doi.org/10.1038/s41467-021-24015-w, 2021.

Böhm, E., Lippold, J., Gutjahr, M., Frank, M., Blaser, P., Antz, B., Fohlmeister, J., Frank, N., Andersen, M. B., and Deininger, M.: Strong and deep Atlantic meridional overturning circulation during the last glacial cycle, Nature, 517, 73–76, 595 https://doi.org/10.1038/nature14059, 2015.

Bourdallé-Badie, R., Lellouche, J.-M., Greiner, E., Hamon, M., Ruggiero, G., Le Galloudec, O., Testut, C.-E., Benkiran, M., Garric, G., Drévillon, M., Parent, L., and Melet, A.: The Mercator Ocean global "blue" ocean reanalysis: past, present, future, Ocean Sciences Meeting 2026 [poster], Zenodo, https://doi.org/10.5281/zenodo.23045545, 2026.

Bryden, H. L., Johns, W. E., King, B. A., McCarthy, G. D., McDonagh, E. L., Moat, B. I., and Smeed, D. A.: Reduction in 600 ocean heat transport at 26° N since 2008 cools the eastern subpolar gyre of the North Atlantic Ocean, J. Climate, 33, 1677–1689, https://doi.org/10.1175/JCLI-D-19-0323.1, 2020.

Buckley, M. W. and Marshall, J.: Observations, inferences, and mechanisms of the Atlantic Meridional Overturning Circulation: a review, Rev. Geophys., 54, 5–63, https://doi.org/10.1002/2015RG000493, 2016.

Carton, J. A., Chepurin, G. A., and Chen, L.: SODA3: a new ocean climate reanalysis, J. Climate, 31, 6967–6983, 605 https://doi.org/10.1175/JCLI-D-18-0149.1, 2018.

Castruccio, F. S.: NCAR/metric: metric v0.1, Zenodo [code], https://doi.org/10.5281/zenodo.4708277, 2021.

https://doi.org/10.5194/egusphere-2026-6871
Preprint. Discussion started: 13 November 2026
© Author(s) 2026. CC BY 4.0 License.

Cunningham, S. A., Kanzow, T., Rayner, D., Baringer, M. O., Johns, W. E., Marotzke, J., Longworth, H. R., Grant, E. M., Hirschi, J. J.-M., Beal, L. M., Meinen, C. S., and Bryden, H. L.: Temporal variability of the Atlantic Meridional Overturning Circulation at 26.5° N, Science, 317, 935–938, https://doi.org/10.1126/science.1141304, 2007.

Cunningham, S. A., Roberts, C. D., Frajka-Williams, E., Johns, W. E., Hobbs, W., Palmer, M. D., Rayner, D., Smeed, D. A., and McCarthy, G. D.: Atlantic Meridional Overturning Circulation slowdown cooled the subtropical ocean, Geophys. Res. Lett., 40, 6202–6207, https://doi.org/10.1002/2013GL058464, 2013.

Danabasoglu, G., Castruccio, F. S., Small, R. J., Tomas, R., Frajka-Williams, E., and Lankhorst, M.: Revisiting AMOC transport estimates from observations and models, Geophys. Res. Lett., 48, e2021GL093045, https://doi.org/10.1029/2021GL093045, 2021.

Danabasoglu, G., Castruccio, F. S., Boza, B., Barthel, A. M., Biastoch, A., Blaker, A., Bozec, A., Bruciaferri, D., Bryan, F. O., Chassignet, E. P., Fu, Y., Grooms, I., Guiavarc'h, C., Hayashida, H., Hogg, A. McC., Holmes, R. M., Iovino, D., Kiss, A. E., Lozier, M. S., Marques, G., Megann, A., Schwarzkopf, F. U., Storkey, D., van Roekel, L., Wolfe, J., Xu, X., and Zhang, R.: Simulated and observed transport estimates across the Overturning in the Subpolar North Atlantic Program (OSNAP) sections, Geosci. Model Dev., 19, 5071–5117, https://doi.org/10.5194/gmd-19-5071-2026, 2026.

Dong, S., Garzoli, S., Baringer, M., Meinen, C., and Goni, G.: Interannual variations in the Atlantic meridional overturning circulation and its relationship with the net northward heat transport in the South Atlantic, Geophys. Res. Lett., 36, L20606, https://doi.org/10.1029/2009GL039356, 2009.

Dong, S., Goni, G., and Bringas, F.: Temporal variability of the South Atlantic meridional overturning circulation between 20° S and 35° S, Geophys. Res. Lett., 42, 7655–7662, https://doi.org/10.1002/2015GL065603, 2015.

ECCO Consortium, Fukumori, I., Wang, O., Fenty, I., Forget, G., Heimbach, P., and Ponte, R. M.: ECCO Ocean Three-Dimensional Volume Fluxes - Monthly Mean llc90 Grid (Version 4 Release 4), Ver. V4r4, NASA Physical Oceanography Distributed Active Archive Center (PO.DAAC) [data set], https://doi.org/10.5067/ECL5M-3VF44, 2021a.

ECCO Consortium, Fukumori, I., Wang, O., Fenty, I., Forget, G., Heimbach, P., and Ponte, R. M.: Synopsis of the ECCO Central Production Global Ocean and Sea-Ice State Estimate (Version 4 Release 4), Zenodo, https://doi.org/10.5281/zenodo.4533349, 2021b.

ECCO Consortium, Fukumori, I., Wang, O., Fenty, I., Forget, G., Heimbach, P., and Ponte, R. M.: ECCO Ocean Temperature and Salinity - Monthly Mean llc90 Grid (Version 4 Release 4), Ver. V4r4, NASA Physical Oceanography Distributed Active Archive Center (PO.DAAC) [data set], https://doi.org/10.5067/ECL5M-OTS44, 2021c.

ECCO Consortium: ECCO Version 4 Python Tutorial, https://ecco-v4-python-tutorial.readthedocs.io/ (last access: 30 July 2026), 2026.

Evans, D. G., Toole, J., Forget, G., Zika, J. D., Naveira Garabato, A. C., Nurser, A. J. G., and Yu, L.: Recent wind-driven variability in Atlantic water mass distribution and meridional overturning circulation, J. Phys. Oceanogr., 47, 633–647, https://doi.org/10.1175/JPO-D-16-0089.1, 2017.

https://doi.org/10.5194/egusphere-2026-6871
Preprint. Discussion started: 13 November 2026
© Author(s) 2026. CC BY 4.0 License.

Evans, D. G., Holliday, N. P., Bacon, S., and Le Bras, I.: Mixing and air–sea buoyancy fluxes set the time-mean overturning circulation in the subpolar North Atlantic and Nordic Seas, Ocean Sci., 19, 745–768, https://doi.org/10.5194/os-19-745-2023, 2023.

Forget, G.: Mapping ocean observations in a dynamical framework: a 2004–06 ocean atlas, J. Phys. Oceanogr., 40, 1201–1221, https://doi.org/10.1175/2009JPO4043.1, 2010.

Forget, G., Campin, J.-M., Heimbach, P., Hill, C. N., Ponte, R. M., and Wunsch, C.: ECCO version 4: an integrated framework for non-linear inverse modeling and global ocean state estimation, Geosci. Model Dev., 8, 3071–3104, https://doi.org/10.5194/gmd-8-3071-2015, 2015.

Fox, A. D., Fraser, N. J., and Cunningham, S. A.: Seasonality of meridional overturning in the subpolar North Atlantic: density flux as a metric for understanding the Atlantic meridional overturning circulation, Ocean Sci., 21, 1735–1760, https://doi.org/10.5194/os-21-1735-2025, 2025.

Frajka-Williams, E., Ansorge, I. J., Baehr, J., Bryden, H. L., Chidichimo, M. P., Cunningham, S. A., Danabasoglu, G., Dong, S., Donohue, K. A., Elipot, S., Heimbach, P., Holliday, N. P., Hummels, R., Jackson, L. C., Karstensen, J., Lankhorst, M., Le Bras, I. A., Lozier, M. S., McDonagh, E. L., Meinen, C. S., Mercier, H., Moat, B. I., Perez, R. C., Piecuch, C. G., Rhein, M., Srokosz, M. A., Trenberth, K. E., Bacon, S., Forget, G., Goni, G., Kieke, D., Koelling, J., Lamont, T., McCarthy, G. D., Mertens, C., Send, U., Smeed, D. A., Speich, S., van den Berg, M., Volkov, D., and Wilson, C.: Atlantic Meridional Overturning Circulation: observed transport and variability, Front. Mar. Sci., 6, 260, https://doi.org/10.3389/fmars.2019.00260, 2019.

Fu, Y., Lozier, M. S., Bower, A., Burmeister, K., Carrilho Biló, T., Cyr, F., Cunningham, S. A., deYoung, B., Dilmahamod, A. F., de Jong, M. F., Fried, N., Holliday, N. P., Fraser, N. J., Johns, W. E., Li, F., Karstensen, J., Pickart, R. S., Straneo, F., and Yashayaev, I.: Characterizing the interannual variability of North Atlantic subpolar overturning, Geophys. Res. Lett., 52, e2025GL114672, https://doi.org/10.1029/2025GL114672, 2025a.

Fu, Y., Lozier, M. S., Bower, A., Burmeister, K., Carrilho Biló, T., Cyr, F., Cunningham, S. A., deYoung, B., Dilmahamod, A. F., de Jong, M. F., Fried, N., Holliday, N. P., Fraser, N., Johns, W. E., Li, F., Karstensen, J., Pickart, R. S., Straneo, F., and Yashayaev, I.: Meridional Overturning Circulation Observed by the Overturning in the Subpolar North Atlantic Program (OSNAP) Array from August 2014 to July 2022, Georgia Institute of Technology [data set], https://doi.org/10.35090/gatech/78023, 2025b.

Garzoli, S. L., Baringer, M. O., Dong, S., Perez, R. C., and Yao, Q.: South Atlantic meridional fluxes, Deep-Sea Res. Pt. I, 71, 21–32, https://doi.org/10.1016/j.dsr.2012.09.003, 2013.

Haines, K., Valdivieso, M., Zuo, H., and Stepanov, V. N.: Transports and budgets in a 1/4° global ocean reanalysis 1989–2010, Ocean Sci., 8, 333–344, https://doi.org/10.5194/os-8-333-2012, 2012.

Hamill, T. M., Whitaker, J. S., and Mullen, S. L.: Reforecasts: an important dataset for improving weather predictions, B. Am. Meteorol. Soc., 87, 33–46, https://doi.org/10.1175/BAMS-87-1-33, 2006.

https://doi.org/10.5194/egusphere-2026-6871
Preprint. Discussion started: 13 November 2026
© Author(s) 2026. CC BY 4.0 License.

Hersbach, H., Bell, B., Berrisford, P., Hirahara, S., Horányi, A., Muñoz-Sabater, J., Nicolas, J., Peubey, C., Radu, R., Schepers, D., Simmons, A., Soci, A., Abdalla, S., Abellan, X., Balsamo, G., Bechtold, P., Biavati, G., Bidlot, J., Bonavita, M., De Chiara, G., Dahlgren, P., Dee, D., Diamantakis, M., Dragani, R., Flemming, J., Forbes, R., Fuentes, M., Geer, A., Haimberger, L., Healy, S., Hogan, R. J., Hólm, E., Janisková, M., Keeley, S., Laloyaux, P., Lopez, P., Lupu, C., Radnoti, G., de Rosnay, P., Rozum, I., Vamborg, F., Villaume, S., and Thépaut, J.-N.: The ERA5 global reanalysis, Q. J. Roy. Meteor. Soc., 146, 1999–2049, https://doi.org/10.1002/qj.3803, 2020.

Jackson, L. C., Kahana, R., Graham, T., Ringer, M. A., Woollings, T., Mecking, J. V., and Wood, R. A.: Global and European climate impacts of a slowdown of the AMOC in a high resolution GCM, Clim. Dynam., 45, 3299–3316, https://doi.org/10.1007/s00382-015-2540-2, 2015.

Jackson, L. C., Dubois, C., Forget, G., Haines, K., Harrison, M., Iovino, D., Köhl, A., Mignac, D., Masina, S., Peterson, K. A., Piecuch, C. G., Roberts, C. D., Robson, J., Storto, A., Toyoda, T., Valdivieso, M., Wilson, C., Wang, Y., and Zuo, H.: The mean state and variability of the North Atlantic circulation: a perspective from ocean reanalyses, J. Geophys. Res.-Oceans, 124, 9141–9170, https://doi.org/10.1029/2019JC015210, 2019.

Johns, W. E., Baringer, M. O., Beal, L. M., Cunningham, S. A., Kanzow, T., Bryden, H. L., Hirschi, J. J.-M., Marotzke, J., Meinen, C. S., Shaw, B., and Curry, R.: Continuous, array-based estimates of Atlantic Ocean heat transport at 26.5° N, J. Climate, 24, 2429–2449, https://doi.org/10.1175/2010JCLI3997.1, 2011.

Kanzow, T., Cunningham, S. A., Rayner, D., Hirschi, J. J.-M., Johns, W. E., Baringer, M. O., Bryden, H. L., Beal, L. M., Meinen, C. S., and Marotzke, J.: Observed flow compensation associated with the MOC at 26.5° N in the Atlantic, Science, 317, 938–941, https://doi.org/10.1126/science.1141293, 2007.

Kanzow, T., Cunningham, S. A., Johns, W. E., Hirschi, J. J.-M., Marotzke, J., Baringer, M. O., Meinen, C. S., Chidichimo, M. P., Atkinson, C., Beal, L. M., and Bryden, H. L.: Seasonal variability of the Atlantic meridional overturning circulation at 26.5° N, J. Climate, 23, 5678–5698, https://doi.org/10.1175/2010JCLI3389.1, 2010.

Karspeck, A. R., Stammer, D., Köhl, A., Danabasoglu, G., Balmaseda, M., Smith, D. M., Fujii, Y., Zhang, S., Giese, B., Tsujino, H., and Rosati, A.: Comparison of the Atlantic meridional overturning circulation between 1960 and 2007 in six ocean reanalysis products, Clim. Dynam., 49, 957–982, https://doi.org/10.1007/s00382-015-2787-7, 2017.

Kersalé, M., Meinen, C. S., Perez, R. C., Le Hénaff, M., Valla, D., Lamont, T., Sato, O. T., Dong, S., Terre, T., van Caspel, M., Chidichimo, M. P., van den Berg, M., Speich, S., Piola, A. R., Campos, E. J. D., Ansorge, I., Volkov, D. L., Lumpkin, R., and Garzoli, S. L.: Highly variable upper and abyssal overturning cells in the South Atlantic, Sci. Adv., 6, eaba7573, https://doi.org/10.1126/sciadv.aba7573, 2020.

Kostov, Y., Johnson, H. L., Marshall, D. P., Heimbach, P., Forget, G., Holliday, N. P., Lozier, M. S., Li, F., Pillar, H. R., and Smith, T.: Distinct sources of interannual subtropical and subpolar Atlantic overturning variability, Nat. Geosci., 14, 491–495, https://doi.org/10.1038/s41561-021-00759-4, 2021.

https://doi.org/10.5194/egusphere-2026-6871
Preprint. Discussion started: 13 November 2026
© Author(s) 2026. CC BY 4.0 License.

Li, F., Lozier, M. S., and Johns, W. E.: Calculating the meridional volume, heat, and freshwater transports from an observing system in the subpolar North Atlantic: observing system simulation experiment, J. Atmos. Ocean. Technol., 34, 1483–1500, https://doi.org/10.1175/JTECH-D-16-0247.1, 2017.

Li, F., Lozier, M. S., Bacon, S., Bower, A. S., Cunningham, S. A., de Jong, M. F., deYoung, B., Fraser, N., Fried, N., Han, G., Holliday, N. P., Holte, J., Houpert, L., Inall, M. E., Johns, W. E., Jones, S., Johnson, C., Karstensen, J., Le Bras, I. A., Lherminier, P., Lin, X., Mercier, H., Oltmanns, M., Pacini, A., Petit, T., Pickart, R. S., Rayner, D., Straneo, F., Thierry, V., Visbeck, M., Yashayaev, I., and Zhou, C.: Subpolar North Atlantic western boundary density anomalies and the Meridional Overturning Circulation, Nat. Commun., 12, 3002, https://doi.org/10.1038/s41467-021-23350-2, 2021.

Lozier, M. S., Li, F., Bacon, S., Bahr, F., Bower, A. S., Cunningham, S. A., de Jong, M. F., de Steur, L., deYoung, B., Fischer, J., Gary, S. F., Greenan, B. J. W., Holliday, N. P., Houk, A., Houpert, L., Inall, M. E., Johns, W. E., Johnson, H. L., Johnson, C., Karstensen, J., Koman, G., Le Bras, I. A., Lin, X., Mackay, N., Marshall, D. P., Mercier, H., Oltmanns, M., Pickart, R. S., Ramsey, A. L., Rayner, D., Straneo, F., Thierry, V., Torres, D. J., Williams, R. G., Wilson, C., Yang, J., Yashayaev, I., and Zhao, J.: A sea change in our view of overturning in the subpolar North Atlantic, Science, 363, 516–521, https://doi.org/10.1126/science.aau6592, 2019.

Lynch-Stieglitz, J., Adkins, J. F., Curry, W. B., Dokken, T., Hall, I. R., Herguera, J. C., Hirschi, J. J.-M., Ivanova, E. V., Kissel, C., Marchal, O., Marchitto, T. M., McCave, I. N., McManus, J. F., Mulitza, S., Ninnemann, U., Peeters, F., Yu, E. F., and Zahn, R.: Atlantic meridional overturning circulation during the Last Glacial Maximum, Science, 316, 66–69, https://doi.org/10.1126/science.1137127, 2007.

McCarthy, G. D., Smeed, D. A., Johns, W. E., Frajka-Williams, E., Moat, B. I., Rayner, D., Baringer, M. O., Meinen, C. S., Collins, J., and Bryden, H. L.: Measuring the Atlantic Meridional Overturning Circulation at 26° N, Prog. Oceanogr., 130, 91–111, https://doi.org/10.1016/j.pocean.2014.10.006, 2015.

Meinen, C. S., Speich, S., Perez, R. C., Dong, S., Piola, A. R., Garzoli, S. L., Baringer, M. O., Gladyshev, S., and Campos, E. J. D.: Temporal variability of the meridional overturning circulation at 34.5° S: results from two pilot boundary arrays in the South Atlantic, J. Geophys. Res. Oceans, 118, 6461–6478, https://doi.org/10.1002/2013JC009228, 2013.

Meinen, C. S., Speich, S., Piola, A. R., Ansorge, I., Campos, E., Kersalé, M., Terre, T., Chidichimo, M. P., Lamont, T., Sato, O. T., Perez, R. C., Valla, D., van den Berg, M., Le Hénaff, M., Dong, S., and Garzoli, S. L.: Meridional overturning circulation transport variability at 34.5° S during 2009–2017: baroclinic and barotropic flows and the dueling influence of the boundaries, Geophys. Res. Lett., 45, 4180–4188, https://doi.org/10.1029/2018GL077408, 2018.

MEOM Group: CDFTOOLS: a Fortran package for analysis and diagnostics on NEMO ocean model output, version 4.0, GitHub [code], https://github.com/meom-group/CDFTOOLS (last access: 30 July 2026), 2026.

Mignac, D., Ferreira, D., and Haines, K.: South Atlantic meridional transports from NEMO-based simulations and reanalyses, Ocean Sci., 14, 53–68, https://doi.org/10.5194/os-14-53-2018, 2018.

Moat, B. I., Smeed, D. A., Rayner, D., Johns, W. E., Smith, R., Volkov, D., Elipot, S., Petit, T., Kajtar, J., Baringer, M. O., and Collins, J.: Atlantic meridional overturning circulation observed by the RAPID-MOCHA-WBTS (RAPID-Meridional

https://doi.org/10.5194/egusphere-2026-6871
Preprint. Discussion started: 13 November 2026
© Author(s) 2026. CC BY 4.0 License.

Overturning Circulation and Heatflux Array-Western Boundary Time Series) array at 26N from 2004 to 2024 (v2024.1a), British Oceanographic Data Centre - Natural Environment Research Council, UK [data set], https://doi.org/10.5285/48d0bf43-0598-ceb2-e063-7086abc062f1, 2026.

Msadek, R., Dixon, K. W., Delworth, T. L., and Hurlin, W.: Assessing the predictability of the Atlantic meridional overturning circulation and associated fingerprints, Geophys. Res. Lett., 37, L19608, https://doi.org/10.1029/2010GL044517, 2010.

Pérez, F. F., Mercier, H., Vázquez-Rodríguez, M., Lherminier, P., Velo, A., Pardo, P. C., Rosón, G., and Ríos, A. F.: Atlantic Ocean CO2 uptake reduced by weakening of the meridional overturning circulation, Nat. Geosci., 6, 146–152, https://doi.org/10.1038/ngeo1680, 2013.

Pita, I., Goes, M., Volkov, D. L., Dong, S., and Schmid, C.: South Atlantic meridional overturning circulation and its respective heat and freshwater transports from sustained observations near 34.5° S, Front. Mar. Sci., 11, 1474133, https://doi.org/10.3389/fmars.2024.1474133, 2024.

Raganato, A., Bracco, A., Van Roekel, L., and Iovino, D.: AMOC discrepancies across reanalyses and models limit dynamical understanding, J. Climate, 39, 5695–5716, https://doi.org/10.1175/JCLI-D-25-0618.1, 2026.

Rousselet, L., Cessi, P., and Forget, G.: Routes of the upper branch of the Atlantic meridional overturning circulation according to an ocean state estimate, Geophys. Res. Lett., 47, e2020GL089137, https://doi.org/10.1029/2020GL089137, 2020.

Rousselet, L., Cessi, P., and Forget, G.: Coupling of the mid-depth and abyssal components of the global overturning circulation according to a state estimate, Sci. Adv., 7, eabf5478, https://doi.org/10.1126/sciadv.abf5478, 2021.

Santer, B. D., Wigley, T. M. L., Boyle, J. S., Gaffen, D. J., Hnilo, J. J., Nychka, D., Parker, D. E., and Taylor, K. E.: Statistical significance of trends and trend differences in layer-average atmospheric temperature time series, J. Geophys. Res. Atmos., 105, 7337–7356, https://doi.org/10.1029/1999JD901105, 2000.

Sinha, B., Smeed, D. A., McCarthy, G., Moat, B. I., Josey, S. A., Hirschi, J. J.-M., Frajka-Williams, E., Blaker, A. T., Rayner, D., and Madec, G.: The accuracy of estimates of the overturning circulation from basin-wide mooring arrays, Prog. Oceanogr., 160, 101–123, https://doi.org/10.1016/j.pocean.2017.12.001, 2018.

Smeed, D. A., Josey, S. A., Beaulieu, C., Johns, W. E., Moat, B. I., Frajka-Williams, E., Rayner, D., Meinen, C. S., Baringer, M. O., and McCarthy, G. D.: The North Atlantic Ocean is in a state of reduced overturning, Geophys. Res. Lett., 45, 1527–1533, https://doi.org/10.1002/2017GL076350, 2018.

Smith, D. M., Cusack, S., Colman, A. W., Folland, C. K., Harris, G. R., and Murphy, J. M.: Improved surface temperature prediction for the coming decade from a global climate model, Science, 317, 796–799, https://doi.org/10.1126/science.1139540, 2007.

Stommel, H.: Thermohaline convection with two stable regimes of flow, Tellus A, 13, 224–230, https://doi.org/10.3402/tellusa.v13i2.9491, 1961.

https://doi.org/10.5194/egusphere-2026-6871
Preprint. Discussion started: 13 November 2026
© Author(s) 2026. CC BY 4.0 License.

Storto, A., Alvera-Azcárate, A., Balmaseda, M. A., Barth, A., Chevallier, M., Counillon, F., Domingues, C. M., Drevillon, M., Drillet, Y., Forget, G., and Garric, G.: Ocean reanalyses: recent advances and unsolved challenges, Front. Mar. Sci., 6, 418, https://doi.org/10.3389/fmars.2019.00418, 2019.

Valdivieso, M., Haines, K., Zuo, H., and Lea, D.: Freshwater and heat transports from global ocean synthesis, J. Geophys. Res. Oceans, 119, 394–409, https://doi.org/10.1002/2013JC009357, 2014.

Vellinga, M. and Wood, R. A.: Global climatic impacts of a collapse of the Atlantic thermohaline circulation, Climatic Change, 54, 251–267, https://doi.org/10.1023/A:1016168827653, 2002.

von Schuckmann, K. and Le Traon, P.-Y. (Eds.): Copernicus Ocean State Report, issue 6, J. Oper. Oceanogr., 15, sup1, 1–220, https://doi.org/10.1080/1755876X.2022.2095169, 2022.

Weijer, W., Cheng, W., Drijfhout, S. S., Fedorov, A. V., Hu, A., Jackson, L. C., Liu, W., McDonagh, E. L., Mecking, J. V., and Zhang, J.: Stability of the Atlantic Meridional Overturning Circulation: a review and synthesis, J. Geophys. Res.-Oceans, 124, 5336–5375, https://doi.org/10.1029/2019JC015083, 2019.

Weijer, W., Cheng, W., Garuba, O. A., Hu, A., and Nadiga, B. T.: CMIP6 models predict significant 21st century decline of the Atlantic Meridional Overturning Circulation, Geophys. Res. Lett., 47, e2019GL086075, https://doi.org/10.1029/2019GL086075, 2020.

Williams, R. G., Katavouta, A., and Roussenov, V.: Regional asymmetries in ocean heat and carbon storage due to dynamic redistribution in climate model projections, J. Climate, 34, 3907–3925, https://doi.org/10.1175/JCLI-D-20-0519.1, 2021.

Winkelbauer, S., Mayer, M., and Haimberger, L.: StraitFlux – precise computations of water strait fluxes on various modeling grids, Geosci. Model Dev., 17, 4603–4620, https://doi.org/10.5194/gmd-17-4603-2024, 2024.

Winkelbauer, S., Winterer, I., Mayer, M., Fu, Y., and Haimberger, L.: Subpolar Atlantic meridional heat transports from OSNAP and ocean reanalyses – a comparison, Ocean Sci., 22, 629–651, https://doi.org/10.5194/os-22-629-2026, 2026.

Yang, C., Bourdallé-Badie, R., and Drévillon, M.: The Marine Environment Reanalyses Evaluation Project MER-EP: towards an improved knowledge of the global ocean environment of the past decades, to support ocean applications and ocean prediction, EGU General Assembly 2026, Vienna, Austria, 3–8 May 2026, EGU26-9403, https://doi.org/10.5194/egusphere-egu26-9403, 2026.

Zhang, R. and Thomas, M.: Horizontal circulation across density surfaces contributes substantially to the long-term mean northern Atlantic Meridional Overturning Circulation, Commun. Earth Environ., 2, 112, https://doi.org/10.1038/s43247-021-00182-y, 2021.

Zhang, R., Sutton, R., Danabasoglu, G., Kwon, Y.-O., Marsh, R., Yeager, S. G., Amrhein, D. E., and Little, C. M.: A review of the role of the Atlantic Meridional Overturning Circulation in Atlantic multidecadal variability and associated climate impacts, Rev. Geophys., 57, 316–375, https://doi.org/10.1029/2019RG000644, 2019.